Photon-pair generation in optical fibers through four-wave mixing: Role of Raman scattering and pump polarization

Q. Lin, F. Yaman, and Govind P. Agrawal
Institute of Optics, University of Rochester, Rochester, New York 14627, USA
(Received 6 September 2006; published 1 February 2007)

We present a general quantum theory capable of describing photon statistics under the combined effects of four-wave mixing and Raman scattering inside optical fibers. Our theory is vectorial in nature and includes all polarization effects. Our analysis shows that spontaneous Raman scattering degrades the pair correlation in all cases but the extent of degradation depends on the pumping configuration employed. In a single-pump configuration, photon pairs can be created with polarization either parallel or orthogonal to the pump. Our results show that the orthogonal configuration can improve the extent of quantum correlation considerably over a broad bandwidth. In the case of a dual-pump configuration, we show that imbalance of two pump powers can be used to improve the quality of photon pairs. We show that orthogonally polarized pumps can generate photon pairs automatically in a polarization-entangled state. In particular, orthogonal pumping with circular polarizations produces such an entangled state with relatively high quality. We also quantify the quality of polarization entanglement as well as energy-time entanglement constructed using correlated photon pairs.

DOI: 10.1103/PhysRevA.75.023803 PACS number(s): 42.50.Dv, 42.65.Lm, 42.65.Yj, 03.67.Mn

I. INTRODUCTION

Entangled photon pairs are essential for quantum technologies requiring delivery of quantum information over significant distances [1]. Conventionally, such photon pairs are generated by spontaneous parametric down conversion [2,3]. Practical implementation of quantum communication requires a photon source with high brightness and relies on its compatibility with fiber-optic networks [4]. Several techniques based on periodically poled lithium niobate waveguides [5,6] have been developed to realize such photon-pair sources.

The phenomenon of four-wave mixing (FWM) occurring inside optical fibers provides a natural way to generate correlated photon pairs in a single spatial mode directly inside fibers [7–17]. Indeed, FWM has been used to realize polarization [18,19] and time-bin [20] entanglement. Although FWM in principle can generate correlated photon pairs with an efficiency higher than other techniques [21–23], in practice, the performance of fiber-based photon-pair sources is severely deteriorated by the phenomenon of spontaneous Raman scattering (SpRS) that accompanies FWM inevitably [24]. SpRS originates from the retarded molecular response to the underlying third-order nonlinearity [25,26], and it leads to a serious limitation on the available range of photon-pair frequencies and the degree of quantum correlation [7–17].

Existing theories cannot describe the impact of SpRS on photon-pair correlation because of a complete neglect of the Raman contribution [21–23]. For this reason, empirical fitting is widely used for the experimental data [7–17]. As FWM becomes a promising way toward creating fiber-based correlated photon sources, it is important to develop a general theory that can explain the experimental data and provide guidance for improving the performance of such sources. In this paper, we develop a general quantum theory capable of describing photon statistics under the combined effects of FWM and Raman scattering inside optical fibers, including both the spontaneous and stimulated contributions. Preliminary results of this study were published recently in Ref. [27]. Moreover, our theory is vectorial in nature and includes all polarization effects. We use this theory to quantify the impact of SpRS on photon-pair generation in various pumping configurations and propose specific schemes for generating photon pairs with high quality.

This paper is organized as follows. In Sec. II, we present the general formalism. We apply it in Sec. III to study photon-pair generation when a single pump beam is launched into a fiber and consider two situations in which the photon pair is polarized either parallel or orthogonal to the pump. Section IV deals with several different dual-pump configurations including when the two pumps are polarized either parallel or orthogonal to each other with linear or circular polarizations. In Sec. V, we investigate the impact of SpRS on the energy-time and polarization entanglement schemes. The final section summarizes the main results of this paper.

II. VECTORIAL QUANTUM THEORY OF FWM

A quantum theory of nonlinear optical phenomenon in optical fibers has been developed before in the context of soliton squeezing [28–30]. Working in the Heisenberg picture with a Hamiltonian that includes the third-order nonlinearity, the two polarization components of the field operator $\hat{A}_i(z,\tau)$ $(i=x,y)$, associated with the slowly varying envelope of the electromagnetic field at the carrier frequency ω_0, are found to satisfy [30]

$$\frac{\partial \hat{A}_i}{\partial z} = i\sum_j \int_{-\infty}^{\tau} d\tau' R_{ij}^{(1)}(\tau-\tau')\hat{A}_j(z,\tau') + i\hbar\omega_0 \sum_{jkl} \int_{-\infty}^{\tau} d\tau' \times R_{ijkl}^{(3)}(\tau-\tau')\hat{A}_k^{\dagger}(z,\tau')\hat{A}_l(z,\tau')\hat{A}_j(z,\tau) + i\sqrt{\hbar\omega_0}\sum_j \hat{m}_{ij}(z,\tau)\hat{A}_j(z,\tau), \quad (1)$$

where $R_{ij}^{(1)}$ describes the linear dispersive properties of the fiber including its birefringence and $R_{ijkl}^{(3)}$ governs various third-order nonlinear effects.

In Eq. (1), the field operator is normalized to have a commutation relation of the form

$$[\hat{A}_j(z,\tau),\hat{A}_k^\dagger(z,\tau')] = \delta_{jk}\delta(\tau-\tau'), \quad j,k=x,y. \tag{2}$$

In our notation, $\hat{A}_j^\dagger(z,\tau)\hat{A}_j(z,\tau)$ represents the operator for the photon flux for the jth polarization component. Further, $\hat{m}_{ij}$ is the noise operator resulting from the presence of a phonon reservoir. Conservation of the commutation relation for the optical field in Eq. (2) at any point z inside the optical fiber requires that the Hermitian operator $\hat{m}_{ij}$ satisfy the following commutation relation:

$$[\hat{m}_{ij}(z,\tau),\hat{m}_{kl}(z',\tau')] = i\delta(z-z')\{R_{klij}^{(3)}(\tau'-\tau) - R_{ijkl}^{(3)}(\tau-\tau')\}. \tag{3}$$

In the case of optical fibers, the third-order nonlinear response function has the general form [31]

$$R_{ijkl}^{(3)}(\tau) = \frac{\gamma}{3}(1-f_R)\delta(\tau)(\delta_{ij}\delta_{kl}+\delta_{ik}\delta_{jl}+\delta_{il}\delta_{jk}) + \gamma f_R R_a(\tau)\delta_{ij}\delta_{kl} + \frac{\gamma}{2}f_R R_b(\tau)(\delta_{ik}\delta_{jl}+\delta_{il}\delta_{jk}), \tag{4}$$

where $R_a(\tau)$ and $R_b(\tau)$ are the isotropic and anisotropic parts of the Raman response, respectively, and f_R represents their fractional contribution to the nonlinear refractive index. The nonlinear parameter $\gamma=n_2\omega_0/(ca_{\text{eff}})$, where a_{eff} is the effective mode area [32]. By substituting Eq. (4) into Eq. (3), the commutation relation for the noise operator takes the form

$$[\hat{m}_{ij}(z,\tau),\hat{m}_{kl}(z',\tau')] = i\gamma f_R\delta(z-z')\left\{[R_a(\tau'-\tau)-R_a(\tau-\tau')]\delta_{ij}\delta_{kl} + \frac{1}{2}[R_b(\tau'-\tau)-R_b(\tau-\tau')](\delta_{ik}\delta_{jl}+\delta_{il}\delta_{jk})\right\}. \tag{5}$$

The simpler scalar form of Eq. (1) has been successfully used to describe quantum squeezing in optical fibers [29,33,34], timing jitter in communication systems [35], and Raman noise in fiber-optic parametric amplifiers [24,36]. Here we use Eq. (1), in its most general vector form, to investigate the impact of SpRS on photon-pair generation through FWM inside optical fibers. As FWM describes nonlinear interaction among multiple optical waves of different frequencies, it is more useful to write Eq. (1) in the spectral domain. Defining the Fourier transform as $\hat{A}_i(z,\omega) = \int_{-\infty}^{\infty}\hat{A}_i(z,\tau)\exp(i\omega\tau)d\tau$, we obtain

$$\frac{\partial\hat{A}_i(z,\omega)}{\partial z} = i\sum_j \tilde{R}_{ij}^{(1)}(\omega)\hat{A}_j(z,\omega) + \frac{i\hbar\omega_0}{(2\pi)^2}\sum_{jkl}\int\int d\omega_1 d\omega_2 \times\tilde{R}_{ijkl}^{(3)}(\omega_2-\omega_1)\hat{A}_k^\dagger(z,\omega_1)\hat{A}_l(z,\omega_2) \times\hat{A}_j(z,\omega+\omega_1-\omega_2) + \frac{i\sqrt{\hbar\omega_0}}{2\pi}\sum_j\int d\omega_1 \times\hat{m}_{ij}(z,\omega-\omega_1)\hat{A}_j(z,\omega_1), \tag{6}$$

where a tilde denotes the Fourier transform and $\hat{m}_{ij}(z,\Omega)$ is a Fourier component of $\hat{m}_{ij}(z,\tau)$ in Eq. (1).

It is easy to show from Eq. (2) that the frequency-domain field operator satisfies the commutation relation

$$[\hat{A}_j(z,\omega_u),\hat{A}_k^\dagger(z,\omega_v)] = 2\pi\delta_{jk}\delta(\omega_u-\omega_v). \tag{7}$$

In the spectral domain, the commutation relation of the noise operator given in Eq. (5) takes the form

$$[\hat{m}_{ij}(z,\Omega_u),\hat{m}_{kl}^\dagger(z',\Omega_v)] = 2\pi\delta(z-z')\delta(\Omega_u-\Omega_v) \times\left\{g_a(\Omega_u)\delta_{ij}\delta_{kl}+\frac{1}{2}g_b(\Omega_u)(\delta_{ik}\delta_{jl}+\delta_{il}\delta_{jk})\right\}, \tag{8}$$

where g_a and g_b are Raman gain or loss coefficients corresponding to the isotropic and anisotropic Raman response functions R_a and R_b, respectively, and they are defined as $g_a(\Omega)=2\gamma f_R\,\text{Im}[\tilde{R}_a(\Omega)]$ and $g_b(\Omega)=2\gamma f_R\,\text{Im}[\tilde{R}_b(\Omega)]$. They are related to the Raman gain measured for linearly copolarized and orthogonally polarized pumps as [31] $g_\parallel=g_a+g_b$ and $g_\perp=g_b/2$. Here, $\tilde{R}_\epsilon(\Omega)$ with $\epsilon=a,b$ is the Fourier transform of $R_\epsilon(\tau)$ defined as $\tilde{R}_\epsilon(\Omega)=\int_{-\infty}^{\infty}R_\epsilon(\tau)\exp(i\Omega\tau)d\tau$. Since $\tilde{R}_a(0)+\tilde{R}_b(0)=1$, the parameter f_R represents the fractional contribution of the Raman response to the nonlinear refractive index [25,26].

Equations (6) and (8) represent the main results of this section. In the following sections, we use them to investigate photon statistics under different pumping configurations. In the case of a photon-pair source, the pumps are always much more intense than the signal and the idler fields. Hence they can be treated classically and assumed to remain undepleted. Moreover, in most experimental situations, the pump pulses are wide enough and fibers are short enough that the dispersion-induced pulse broadening is negligible. As a result, the pumps can be assumed to be quasicontinuous such that $A_j(z,\omega)=A_{pj}(z)2\pi\delta(\omega-\omega_p)$, where ω_p is the pump frequency. For convenience, we renormalize the pump field amplitude such that $|A_{pj}|^2$ provides the pump power of the jth polarization component at ω_p. As short fibers are generally used for photon generation, we neglect fiber losses in the following analysis.

III. SINGLE-PUMP CONFIGURATION

In this section, we focus on the case in which FWM is induced by a single pump wave launched at ω_p. Energy conservation requires $2\omega_p=\omega_s+\omega_i$, where ω_s and ω_i are frequen-

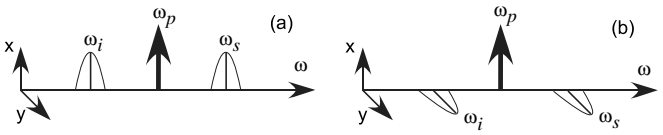

FIG. 1. Illustration of the relative frequencies and polarizations for the pump, signal, and idler in the single-pump configuration.

cies of signal and idler photons, respectively. We assume that the pump is linearly polarized along a principal axis of the fiber, say, the x axis. It is easy to show [32] that the Kerr nonlinearity only imposes a phase modulation on the pump wave such that $A_{px}(z)=A_p\Phi(z)$, where $\Phi(z)=\exp\{i[k_x(\omega_p)+\gamma P_0]z\}$, A_p is the input pump field amplitude, $P_0=|A_p|^2$ is the pump power, and $k_x(\omega_p)\equiv\tilde{R}^{(1)}_{xx}(\omega_p)$ is the propagation constant.

A. Signal and idler evolution

It turns out that the FWM process can be decoupled into two independent "eigen" processes shown in Fig. 1 such that the created photon pairs are polarized either (a) parallel or (b) orthogonal to the pump. Of course, the phase-matching conditions for these two processes are not the same. The process (a) is phase-matched in practice through fiber dispersion by appropriately locating the pump wavelength. In contrast, the process (b) is affected by fiber birefringence [32]. We discuss the phase-matching issue in more detail in Sec. III D.

If we use $\omega=\omega_s$ in Eq. (6) and retain only the first order terms at this frequency and at its conjugate frequency $\omega_i=2\omega_p-\omega_s$, we obtain the Heisenberg equations for the two polarization components of the signal in the form

$$\frac{\partial\hat{A}_j(z,\omega_s)}{\partial z}=i[k_j(\omega_s)+\gamma\xi_j(\Omega_{\rm sp})P_0]\hat{A}_j(z,\omega_s)+i\gamma\eta_j(\Omega_{\rm sp})A_{px}^2\hat{A}_j^\dagger(z,\omega_i)+iA_{px}\hat{m}_{jx}(z,\Omega_{\rm sp}),\tag{9}$$

where $j=x,y$ for the process of Figs. 1(a) and 1(b), respectively, $k_j(\omega_s)=\tilde{R}^{(1)}_{jj}(\omega_s)$ is the propagation constant at frequency ω_s, and $\Omega_{\rm sp}=\omega_s-\omega_p$ is the signal-pump frequency separation. The idler equation can be obtained by exchanging the subscripts s and i.

The complex quantities ξ_x and ξ_y take into account the nonlinear phase shift produced by the pump through cross-phase modulation as well as the effects of Raman scattering. They are given by

$$\xi_x(\Omega_{\rm sp})=2-f_R+f_R\tilde{R}_a(\Omega_{\rm sp})+f_R\tilde{R}_b(\Omega_{\rm sp}),\tag{10}$$

$$\xi_y(\Omega_{\rm sp})=2(1-f_R)/3+f_R\tilde{R}_a(0)+f_R\tilde{R}_b(\Omega_{\rm sp})/2.\tag{11}$$

The Raman effects enter through $\tilde{R}_a$ and $\tilde{R}_b$, as discussed in Sec. II. In the absence of Raman contribution ($f_R=0$), $\xi_x=2$ and $\xi_y=2/3$, as expected from the standard theory of cross-phase modulation [32]. Also note that $\xi_x(0)=2$ even when Raman contribution is included because $\tilde{R}_a(0)+\tilde{R}_b(0)=1$.

The FWM efficiency is related to η_j and is different for the two eigenprocesses. More specifically,

$$\eta_x(\Omega_{\rm sp})=(1-f_R)+f_R\tilde{R}_a(\Omega_{\rm sp})+f_R\tilde{R}_b(\Omega_{\rm sp}),\tag{12}$$

$$\eta_y(\Omega_{\rm sp})=(1-f_R)/3+f_R\tilde{R}_b(\Omega_{\rm sp})/2.\tag{13}$$

In practice, the first term dominates, indicating that copolarized FWM is roughly three times more efficient than the orthogonally polarized one. For this reason, most recent experiments have focused on the copolarized configuration [7–16]. However, this approach has a serious drawback because SpRS is also maximized when the signal and idler are copolarized with the pump. Moreover, the Raman process also changes the refractive index through the Kramers-Kronig relation and thus affects the FWM efficiency [26]. The magnitude of η_x decreases by about 20% when the signal is detuned far beyond Raman gain peak. In contrast, η_y exhibits much less dependence on $\Omega_{\rm sp}$ because of relatively small Raman scattering from the orthogonally polarized pump. This will be discussed in detail in the following subsections.

Equation (9) in combination with the corresponding idler equation can be solved analytically because of their linear nature. The resulting solution for the signal amplitude at the end of a fiber of length L is given by

$$\hat{A}_j(L,\omega_s)=[\alpha_j(L,\omega_s)\hat{A}_j(0,\omega_s)+\beta_j(L,\omega_s)\hat{A}_j^\dagger(0,\omega_i)+\hat{N}_j(L,\omega_s)]\Phi(L),\tag{14}$$

where the first two terms are due to FWM but the last one describes the impact of Raman scattering. The coefficients appearing in this equation are given by [32]

$$\alpha_j(L,\omega_s)=[\cosh(g_jL)+(i\kappa_j/2g_j)\sinh(g_jL)]e^{iK_jL},\tag{15}$$

$$\beta_j(L,\omega_s)=(i\gamma\eta_j/g_j)A_p^2\sinh(g_jL)e^{iK_jL},\tag{16}$$

$$\hat{N}_j(L,\omega_s)=i\int_0^L\hat{m}_{jx}(z,\Omega_{\rm sp})[A_p\alpha_j(L-z,\omega_s)-A_p^*\beta_j(L-z,\omega_s)]dz,\tag{17}$$

where the parametric gain coefficient g_j is given by $g_j^2=(\gamma\eta_jP_0)^2-(\kappa_j/2)^2$ and $K_j=[k_j(\omega_s)-k_j(\omega_i)]/2$. Further, the extent of phase mismatch is governed by

$$\kappa_j=k_j(\omega_s)+k_j(\omega_i)-2k_x(\omega_p)+2\gamma P_0(\xi_j-1).\tag{18}$$

In practice, the signal and idler fields are filtered spectrally to limit their bandwidth using an optical filter. The filtered field can be written as

$$\hat{A}_{uj}(z,\tau)=\frac{1}{2\pi}\int_{-\infty}^{\infty}H_u(\omega-\bar{\omega}_u)\hat{A}_j(z,\omega)\exp(-i\omega\tau)d\omega,\tag{19}$$

where $H_u(\omega-\bar{\omega}_u)$ is the filter transmission function centered at $\bar{\omega}_u$ $(u=s,i)$ and assumed to be polarization independent. In

the following discussion, we denote the signal as the anti-Stokes wave and assume $\bar{\omega}_s > \omega_p$. The idler field then lies, by definition, on the Stokes side of the pump.

B. Photon-pair generation rate

As the two FWM processes in Fig. 1 have the same form of solution, we simplify the following analysis by dropping the polarization subscript j in Eqs. (14)–(19). The two cases shown in Fig. 1 can be compared by choosing the appropriate form of ξ_j, η_j, κ_j, and g_j with $j=x$ or y. The generation rate of photon pairs is related to the photon flux I_u, defined as $I_u \equiv \langle \hat{A}_u^\dagger(L,\tau)\hat{A}_u(L,\tau)\rangle$, where $u=s$ for signal photons, $u=i$ for idler photons, and the angle brackets denote average with respect to the vacuum input state and a thermally populated phonon reservoir. Such an average can be performed analytically and results in the following expression:

$$I_u = \frac{1}{2\pi}\int_{-\infty}^{\infty} |H_u|^2 \{|\beta_u|^2 + \mathcal{N}(\Omega_{up})\mathrm{sgn}(\Omega_{up}) \times [1 + |\beta_u|^2 - |\alpha_u|^2]\} d\omega_u, \tag{20}$$

where $H_u \equiv H_u(\omega_u - \bar{\omega}_u)$, $\alpha_u \equiv \alpha(L,\omega_u)$, $\beta_u \equiv \beta(L,\omega_u)$, $\mathrm{sgn}(\Omega_{uv}) = \pm 1$ depending on the sign of Ω_{uv}, and

$$\mathcal{N}(\Omega_{uv}) = \begin{cases} n(\Omega_{uv}) & \text{when } \Omega_{uv} > 0, \\ n(\Omega_{uv}) + 1 & \text{when } \Omega_{uv} < 0. \end{cases} \tag{21}$$

Here $n(\Omega_{uv}) = [\exp(\hbar|\Omega_{uv}|/k_B T) - 1]^{-1}$ is the phonon population at frequency $\Omega_{uv} = \omega_u - \omega_v$ and at temperature T. As the magnitude of β in Eq. (16) is determined by the phase-matching condition, photon flux peaks at the location where this condition is satisfied.

Equation (20) is quite general as it includes both the spontaneous and stimulated processes. For correlated photon-pair generation, the pump power is kept low enough that $\gamma P_0 L \ll 1$ to prevent stimulated scattering. Moreover, the filters have a bandwidth much narrower than the phase-matching bandwidth and are positioned at the center of the phase-matching window where $\mathrm{Re}(\kappa) \approx 0$. In this case, Eq. (20) reduces to

$$I_u = \Delta\nu_u(|\gamma P_0 \eta_u L|^2 + P_0 L |g_R| \mathcal{N}_{up}), \tag{22}$$

where η_u, g_R, and $\mathcal{N}_{up}$ are calculated at the frequency $\bar{\Omega}_{up} = \bar{\omega}_u - \omega_p$ $(u=s,i)$ and the filter bandwidth $\Delta\nu_u$ is defined as $\Delta\nu_u = \int |H_u(\omega - \bar{\omega}_u)|^2 d\omega/2\pi$. Further, $g_R = g_\parallel$ and $g_\perp$ for the processes shown in Figs. 1(a) and 1(b), respectively.

When pump pulses of duration of τ_p at a repetition rate of B are used (for a continuous pump, $\tau_p B = 1$), the photon counting rate is related to I_u as $\mathcal{R}_u = (\zeta_u \tau_p B) I_u$ [21], where ζ_u is the detection efficiency. As expected, the photon counting rate consists of two terms: One originates from FWM and grows quadratically with both pump power P_0 and fiber length L; the other is due to SpRS and grows only linearly with the product $P_0 L$.

Figure 2 shows the normalized photon flux, defined as $I_\mu/\Delta\nu_\mu$, at a typical pumping level of $\gamma P_0 L = 0.1$. This value corresponds to a 1.25 GHz photon flux created by FWM

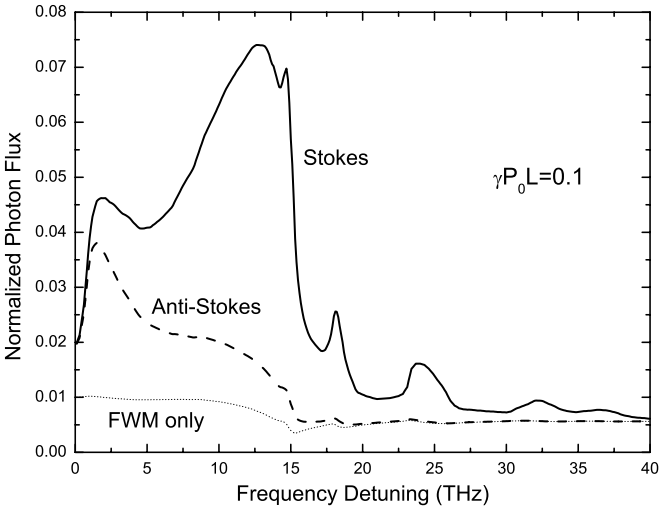

FIG. 2. Normalized photon flux as a function of pump-signal detuning. The solid and dashed curves show photon flux for idler (Stokes) and signal (anti-Stokes), respectively. The two fluxes are the same (thin dotted curve) when they are created by FWM alone [the first term in Eq. (22)].

with a continuous-wave pump and a 1 nm filter at 1550 nm. The fiber parameters used in the 1550 nm regime are $n_2 = 2.6 \times 10^{-20}$ m^2/W, a peak Raman gain of 0.62×10^{-13} m/W [32,37,38], and a temperature of $T = 300$ K. The Raman spectra are taken from Ref. [25]. The photon pair is assumed to be copolarized with the pump. When $|\bar{\Omega}_{up}|/2\pi < 1$ THz, the phonon population $n(\bar{\Omega}_{up}) \gg 1$ and SpRS generates a similar amount of signal and idler photons. When $|\bar{\Omega}_{up}|/2\pi > 4$ THz, $n(\bar{\Omega}_{up}) \ll 1$ and SpRS creates much more noise photons on the idler (Stokes) than the signal (anti-Stokes). Moreover, below 15 THz frequency detuning, SpRS noise photon flux is significantly larger than that created by FWM in both signal and idler, especially in the low-frequency regime. It is negligible for the signal detuned beyond 15 THz, but it still contributes considerably to the idler located on the Stokes side. Although the dominance of SpRS can be reduced by increasing the pump power, this approach reduces the photon-pair quality significantly because of an increase in stimulated FWM (see next section). For this reason, SpRS remains a dominant degradation source for the correlated photon pairs generated within the Raman gain bandwidth.

C. Self- and cross-correlation coefficients

An important way to characterize the quality of a photon-pair source is the degree of quantum correlation, given by the ratio between the true coincidence counting and the accidental one. Consider first the self-correlation coefficient of the signal (or idler) photons defined as [39]

$$\rho_u(\tau) = \langle \hat{A}_u^\dagger(L,t)\hat{A}_u^\dagger(L,t+\tau)\hat{A}_u(L,t+\tau)\hat{A}_u(L,t)\rangle / I_u^2 - 1, \tag{23}$$

where $u=s$ and i for the signal and idler photons, respectively. As before, the average can be calculated analytically using Eqs. (14)–(19) to yield

$$\rho_u(\tau) = \frac{1}{(2\pi I_u)^2}\left| \int_{-\infty}^{\infty} |H_u|^2[|\beta_u|^2 + \mathcal{N}(\Omega_{up})\mathrm{sgn}(\Omega_{up}) \times (1 + |\beta_u|^2 - |\alpha_u|^2)]e^{-i\omega_u\tau}d\omega_u \right|^2. \quad (24)$$

For optical filters with a bandwidth much narrower than the phase-matching bandwidth, α_u and β_u can be treated as constant. In this case, the self-correlation coefficient reduces to a remarkably simple expression $\rho_u(\tau)=|\varphi_u(\tau)|^2$, where $\varphi_u(\tau)$ is the autocorrelation function of the filter response defined as

$$\varphi_u(\tau) = \frac{1}{2\pi\Delta\nu_u}\int_{-\infty}^{\infty} |H_u(\omega_u - \bar{\omega}_u)|^2 e^{-i\omega_u\tau}d\omega_u. \quad (25)$$

It is easy to show that $\rho_u(\tau) \leqslant \rho_u(0)=1$. Thus the signal as well as the idler photons exhibit the bunching effect, irrespective of whether they are created through FWM or SpRS. This is expected as spontaneously generated photons are of a thermal distribution for individual signal (or idler) wave [1,39,60]. Indeed, their thermally distributed nature is directly reflected in Eq. (24), which can be written in the simple form $\rho_u(\tau)=|\langle \hat{A}_u^\dagger(L,t+\tau)\hat{A}_u(L,t)\rangle|^2/I_u^2$.

Because of the photon-bunching feature of spontaneous scattering (for both FMW and SpRS), a Hanbury-Brown–Twiss type experiment performed for measuring self-correlation cannot be used to test the dominance of single photons or to show the existence of SpRS. Note that the self-correlation is also independent of pump power when narrow band filters are used. The decrease in the experimentally recorded values at low pump powers observed in Ref. [16] is likely due to dark counting.

Although photons generated by FWM as well as SpRS follow a thermal distribution, FWM-generated signal photons are strongly correlated with the idler photons but SpRS-generated ones are not, since FWM-created photons are in a two-mode squeezed state [39,60]. This quantum correlation between the signal and idler photons is quantified by the cross-correlation coefficient defined as [39]

$$\rho_c(\tau) = \langle \hat{A}_i^\dagger(L,t)\hat{A}_s^\dagger(L,t+\tau)\hat{A}_s(L,t+\tau)\hat{A}_i(L,t)\rangle/(I_sI_i) - 1, \quad (26)$$

where $\langle \hat{A}_i^\dagger(L,t)\hat{A}_s^\dagger(L,t+\tau)\hat{A}_s(L,t+\tau)\hat{A}_i(L,t)\rangle$ is the biphoton probability of the signal-idler pair. By using Eqs. (14)–(17), the pair correlation in its most general form is given by

$$\rho_c(\tau) = \frac{1}{(2\pi)^2 I_s I_i}\left| \int_{-\infty}^{\infty} \mathcal{H}(\omega_s)[\alpha_i\beta_s + \mathcal{N}(\Omega_{\mathrm{sp}})\mathrm{sgn}(\Omega_{\mathrm{sp}}) \times (\alpha_i\beta_s - \alpha_s\beta_i)]e^{-i\omega_s\tau}d\omega_s \right|^2, \quad (27)$$

where $\mathcal{H}(\omega_s) \equiv H_s(\omega_s - \bar{\omega}_s)H_i(\omega_i - \bar{\omega}_i)$ with $\omega_i = 2\omega_p - \omega_s$. As the magnitudes of α and β are maximized when the FWM efficiency is maximum, ρ_c peaks when the center frequencies of the two filters are tuned to the centers of the phase-matched spectral window with $\bar{\omega}_s + \bar{\omega}_i = 2\omega_p$. The magnitude of ρ_c decreases when either filter is detuned away from this condition, as also observed experimentally in Refs. [15,16]. It turns out that Eq. (27) can be written in a simple form of $\rho_c(\tau)=|\langle \hat{A}_s(L,t+\tau)\hat{A}_i(L,t)\rangle|^2/(I_sI_i)$. This is a direct result of the thermally distributed nature of spontaneous scattering.

The general expression in Eq. (27) can be used to find the quantum correlation under low-power conditions such that $\gamma P_0 L \ll 1$. Far from the phase-matching condition ($|\Delta kL| \gg 1$), FWM becomes negligible, and SpRS dominates. In this case, Eq. (27) reduces to

$$\rho_c(\tau) = |\varphi_c(\tau)|^2\left[\frac{\sin(\Delta kL/2)}{\Delta kL/2}\right]^2 \frac{\gamma^2|\mathrm{Re}(\eta_s)/g_R|^2 + (n+1/2)^2}{n(n+1)}, \quad (28)$$

where $\Delta k = k(\omega_s) + k(\omega_i) - 2k(\omega_p)$ is the linear phase mismatch and $\varphi_c(\tau)$ is the cross-correlation of the two filter responses defined as

$$\varphi_c(\tau) = \frac{1}{2\pi\sqrt{\Delta\nu_s\Delta\nu_i}}\int_{-\infty}^{\infty} H_s(\omega - \bar{\omega}_s)H_i(\bar{\omega}_s - \omega)e^{-i\omega\tau}d\omega. \quad (29)$$

Clearly, $\rho_c \to 0$ for $|\Delta kL| \gg 1$, indicating independent creation of the signal and idler photons. This is expected in view of the fact that they are generated from thermal phonon states.

To generate correlated photon pairs, the signal and idler are tuned to the phase-matching peak. Equation (27) in this case reduces to

$$\rho_c(\tau) = \frac{|\varphi_c(\tau)|^2\{[\gamma\,\mathrm{Re}(\eta_s)]^2 + |g_R(n+1/2)|^2\}}{[|\gamma\eta_s|^2 P_0 L + |g_R|(n+1)][|\gamma\eta_s|^2 P_0 L + |g_R|n]}. \quad (30)$$

The pair correlation decreases with increased pump power because of an increased probability of multiphoton generation, as observed experimentally [10,15,16]. SpRS introduces considerable accidental coincidence counting and thus reduces the correlation magnitude. For a pure FWM process without SpRS, η_s is real and the pair correlation reduces to $\rho_c(\tau)=|\varphi_c(\tau)|^2/|\gamma\eta_s P_0 L|^2$.

D. Comparisons of the two processes in Fig. 1

Figure 3 shows $\rho_c(0)$ as a function of pump-signal detuning for the two polarization configurations of Fig. 1 at a typical pumping level of $\gamma P_0 L = 0.1$, assuming an identical shape for the two optical filters so that $|\varphi_c(0)|^2=1$. As mentioned earlier in a previous section, the FWM efficiency is reduced roughly by a factor of 3 in the case of orthogonal configuration. For a fair comparison of the two configurations, we increased the input pump power P_0 by a factor of 3 in the orthogonal case to ensure that FWM creates nearly the same number of photons in the two cases.

Several conclusions can be drawn from Fig. 3. In general, SpRS degrades pair correlation over a broad spectral range extending from 0 to 40 THz when the photon pair is copolarized with the pump (dashed curves). Even when the signal is close to the pump (frequency detuning <1 THz) and is far

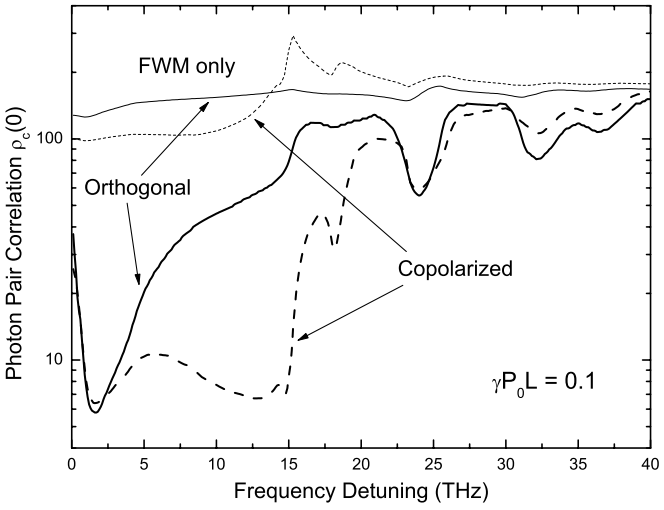

FIG. 3. Pair correlation $\rho_c(0)$ versus pump-signal detuning, assuming perfect phase matching and using the same parameter values used for Fig. 2. The dashed and solid curves show the cases in which photons are copolarized and orthogonally polarized to the pump, respectively. The two thin curves show for comparison the case when FWM acts alone (no SpRS). A slight difference between them is due to different Raman-induced changes to n_2.

away from the Raman peak, pair correlation is reduced by more than 50%, compared with a pure FWM process (thin dashed curve), because of high phonon population around this region. For example, Eq. (30) shows that pair correlation is about 12 at a frequency detuning of 0.5 THz for a typical value of $\gamma P_0 L=0.15$ but it reduces to 3.5 when $\gamma P_0 L$ increases to 0.4, indicating that the recent experiments in this regime are operating close to the fundamental limit set by SpRS [9,10,15]. For frequency detunings >2 THz, the magnitude of copolarized Raman gain grows rapidly and leads to more SpRS-created idler photons, even though SpRS creates less signal photons because of a reduction in the phonon population (see Fig. 2). As a result, the accidental coincidence counting rate becomes large in the copolarized case (dashed curves), and the correlation drops to a rather low value over a broad spectral range extending from 2 to 15 THz. This degradation is a direct consequence of the enhanced SpRS in the copolarized configuration of Fig. 1.

As seen in Fig. 3, $\rho_c(0)$ increases to high values when the signal is detuned far beyond the Raman-gain peak (but with an $\sim$40% reduction in the FWM-generated photons because of a Raman-induced decrease in the FWM efficiency; see Fig. 2). SpRS has only a minor effect in this spectral region. For example, near 30 THz, $\rho_c(0)$ varies from 39 to 138 for $\gamma P_0 L$ in the range of 0.1–0.2; it can be increased to 450 when $\gamma P_0 L$ is decreased to 0.05. For this reason, several experiments have been designed to operate in this regime [11,12,16]. As an example, consider the data of Ref. [16]. With a pump-signal detuning of 28 THz near 735 nm, Eq. (30) shows that $\rho(0)=2105$, 42, and 17 for $\gamma P_0 L=0.0155$, 0.19, and 0.31, respectively (corresponding to average power levels of 0.05, 0.6, and 1 mW in Ref. [16], respectively). These values are higher than the experimentally measured correlation of 300, 23, and 10 at these power levels, implying the possibility of further experimental improvement in this spectral regime.

A relatively large difference between the theoretical and experimental values of $\rho_c(0)$ at the lowest power level can be attributed to dark counting that tends to dominate at low photon-detection rates [20]. In practice, the photon counting rate is given by $\mathcal{R}'_u=\mathcal{R}_u+\mathcal{R}_{du}$ $(u=s,i)$, where $\mathcal{R}_{du}$ is the dark count rate. The presence of dark counts increases the accidental coincidence counting rate given by $\mathcal{R}_{ac}(\tau_0)=\int_{\tau_0}^{\tau_0+\tau_c}\mathcal{R}'_s\mathcal{R}'_i d\tau$, where τ_c is the coincidence time window. However, it does not affect the true coincidence counting rate provided by $\mathcal{R}_{tc}(\tau_0)=\zeta_s\zeta_i\tau_p B\int_{\tau_0}^{\tau_0+\tau_c} I_s I_i \rho_c(\tau)d\tau$. The experimental recorded value $\rho'_c(\tau)$ is the ratio $\mathcal{R}_{tc}/\mathcal{R}_{ac}$. If the real photon detection rate dominates $(\mathcal{R}_u \gg \mathcal{R}_{du})$, ρ'_c would be close to ρ_c given in Eqs. (27) and (30). However, if $\mathcal{R}_u < \mathcal{R}_{du}$ at low pump levels, ρ'_c would be significantly lower than ρ_c.

Figure 3 shows that high-quality photon pairs can be generated with copolarized FWM only when the signal is far from the pump (detuning >20 THz). However, the quality of photon pairs can be maintained at a high level over a broad spectral region below 20 THz when they are generated with polarization orthogonal to the pump (solid curves). This improvement is due to the fact that the Raman gain is almost negligible in the orthogonal configuration [25], a feature that improves $\rho_c(0)$ considerably. The most improvement occurs in the detuning range of 5 to 15 THz, the same range where the copolarized configuration is the worst. Near the copolarized Raman-gain peak close to 13 THz, the quantum correlation can be increased from a value of 7 to more than 60 for $\gamma P_0 L=0.1$. The negligible Raman scattering not only reduces SpRS dramatically in this configuration, but also introduce much less dispersion on nonlinear refractive index and thus has much less impact on FWM efficiency, leading to a FWM-created photon flux nearly independent of frequency detuning. This can be seen by the pair correlation for the pure FWM (thin solid curve), which exhibits much less frequency dependence compared with the copolarized process (thin dashed curve).

In practice, phase matching in the orthogonal configuration of FWM [Fig. 1(b)] can be realized using low-birefringence fibers [40,41]. Equation (18) shows that the phase mismatch depends on both the birefringence and even-order dispersion parameters at the pump frequency as

$$\kappa_y = k_y(\omega_s)+k_y(\omega_i)-2k_x(\omega_p)+2\gamma P_0(\xi_y-1)$$
$$=\frac{2\omega_p}{c}\delta n+2\sum_{m=1}^{\infty}\frac{\beta_{2m}\Omega_{sp}^{2m}}{(2m)!}+2\gamma P_0(\xi_y-1), \qquad (31)$$

where $\delta n=n_y(\omega_p)-n_x(\omega_p)$ is the birefringence and β_{2m} is the $(2m)$th-order dispersion parameter at ω_p along the y axis. In the low-power regime, the nonlinear phase shift (last term) has a negligible effect on the phase-matching condition. Figure 4 shows examples of phase-matched pump-signal detuning as a function of pump wavelength for fibers with different magnitudes of birefringence using $\beta_3=0.06541$ ps^2/km, $\beta_4=-1.0383\times10^{-4}$ ps^4/km, $\beta_5=3.3756\times10^{-7}$ ps^5/km, $\beta_6=-1.1407\times10^{-10}$ ps^6/km, and $\gamma=23$ W^{-1}/km at the zero-

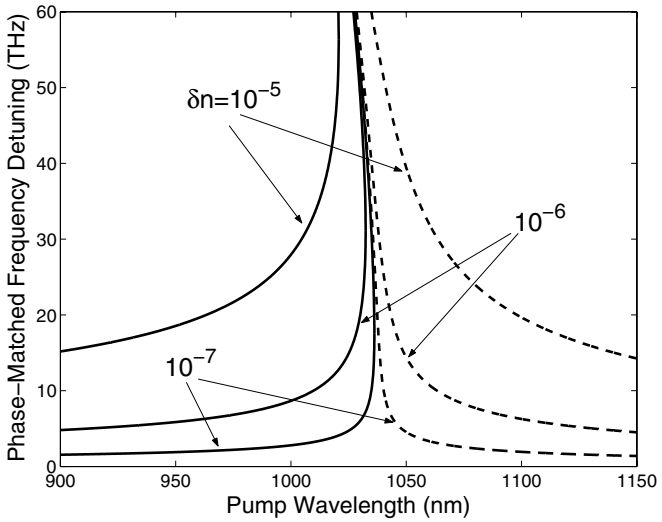

FIG. 4. Phase matching curves as a function of pump wavelength. The pump launched at the slow axis ($\delta n<0$) for solid curves and along the fast axis ($\delta n>0$) for dashed curves. Fiber dispersion is assumed to be the same for both axes.

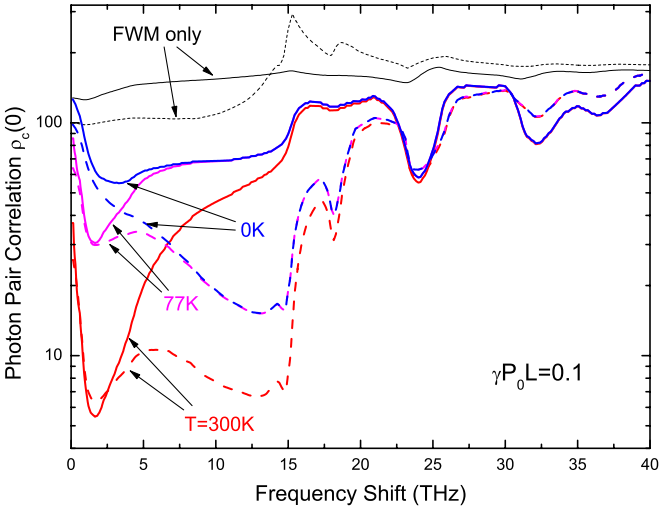

FIG. 5. (Color online) Pair correlation $\rho_c(0)$ versus pump-signal detuning for several fiber temperatures, assuming perfect phase matching and using fiber parameters used for Fig. 2. The dashed and solid curves show the copolarized and orthogonally polarized cases, respectively. The two thin curves show the case of pure FWM (no SpRS).

dispersion wavelength of 1038 nm [42]. Clearly, the phase-matching condition can be satisfied for a variety of pump-signal detunings by tuning the pump wavelength and pump polarization. Note that conventional fibers with random birefringence cannot be used for realizing the orthogonal configuration because the polarizations of the pump, signal, and idler change in a random manner when a long fiber is employed [43,44]. In practice, a fiber with random birefringence can be used only if its length is shorter than the birefringence correlation length.

In this case of an orthogonally polarized FWM process [Fig. 1(b)], SpRS still creates noise photons that are copolarized with the pump, but this noise background can be removed by simply placing polarizers oriented orthogonal to the pump before the signal and idler photons reach the detectors. It is important to stress that, although the signal and idler fields are polarized orthogonal to the pump polarization, their spectra remain symmetric, as dictated by the phase-matching condition in Eq. (31). Thus our proposed scheme does not suffer from the distinguishability induced by spectral asymmetry when type-II phase matching is used for $\chi^{(2)}$-based devices [45,46]. One issue that needs to be addressed is the amount of walk off between the pump and signal or idler; it can be controlled in practice by using longer pump pulses.

E. Effect of fiber temperature

Equations (22) and (30) show that the SpRS-created noise photon and its impact on pair correlation are both related to the phonon population, which strongly depends on fiber temperature. Hence SpRS can be significantly reduced by cooling the fiber, as recently demonstrated in experiments [13,14]. Figure 5 shows pair correlation at three temperatures. As phonon population inversely exponentially depends on pump-signal frequency detuning, it has a large effect at low frequency detuning, leading to strong temperature dependence below 5 THz. By reducing the fiber temperature to that of liquid nitrogen at 77 K, pair correlation can be enhanced by up to five times around this regime. However, it has negligible effect when frequency detuning is large. Moreover, SpRS cannot be completely eliminated by reducing the temperature. This can be seen by the curves at zero temperature, where SpRS still remains a significant effect over a broad spectral region. This is because SpRS for the idler at the Stokes side is dominantly coupled to the ground state of the phonon, which always introduces noise photons irrespective of fiber temperature, although SpRS can be nearly eliminated for the signal at the anti-Stokes side.

IV. DUAL-PUMP CONFIGURATION

One advantage of FWM in optical fibers compared with a $\chi^{(2)}$-based process is that it allows for the use of two pumps with different frequencies and polarization states, which provides more quantum functionalities. In fact, a dual-pump configuration is used routinely for classical, fiber-based, parametric amplification and wavelength conversion [47–50]. When the pumps are copolarized, the dual-pump configurations, shown schematically in Fig. 6, may offer some advantages. For example, unlike the single-pump con-

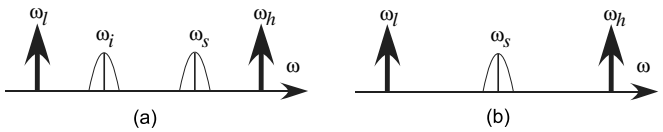

FIG. 6. Configuration with linear pump polarizations parallel to each other. The signal and idler photons are (a) distinguishable or (b) indistinguishable on the basis of their frequencies.

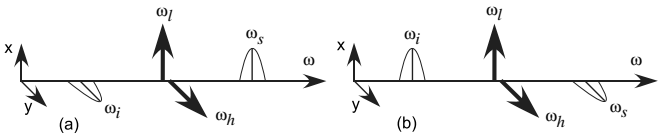

FIG. 7. Configuration with linear pump polarizations orthogonal to each other, showing the frequency and polarization relationships among the pumps, signal, and idler.

figuration in which the signal and idler photons are always created on opposite sides of the pump frequency, and are thus distinguishable on the basis of their frequencies, two photons can be created at the same frequency by placing a filter at the center frequency of the two pumps [15] [see Fig. 6(b)].

When two separate pump beams are used, it becomes possible to align the polarizations of two pumps orthogonal to each other, as shown schematically in Fig. 7. This scheme is often used for polarization-independent operation of a classical parametric amplifier [47,49]. Because of a spin-conservation requirement for the four interacting photons, the signal and idler photons must also be orthogonally polarized, although their individual state of polarizations (SOPs) can be arbitrary [51]. This feature provides a simple way to realize polarization entanglement automatically. In this section, we investigate the general case in which two pumps are launched into an optical fiber for creating correlated photon pairs. We focus on three typical pumping configurations where the two pump SOPs are either linearly parallel, linearly orthogonal, or circularly orthogonal.

A. Signal and idler equations

We consider first that the two pumps are of linear SOPs. We assume that the two pumps at frequencies ω_l and ω_h are launched either along a principal axis of a birefringent fiber (say, the x axis) for copolarized pumping or along two principal axes for orthogonal pumping. In the latter case, we assume the low-frequency pump is polarized along the x axis, as shown in Fig. 7. In both cases, the two pumps maintain their SOPs along the fiber. Unlike the case of a single pump discussed in Sec. III, the two pumps can interact with each other through the fiber nonlinearity. From Eq. (6), the pump fields, $A_{lx}(z)$ and $A_{hx}(z)$ [or $A_{hy}(z)$, depending on pumping configuration] are found to satisfy

$$\frac{\partial A_{uj}}{\partial z} = i[k_j(\omega_u) + \gamma P_u + \gamma \xi_q(\Omega_{uv}) P_v] A_{uj}, \tag{32}$$

where $u \neq v$ and $\Omega_{uv} = \omega_u - \omega_v$. The subscripts $j=q=x$ for copolarized pumps. In the case of orthogonally polarized pumps, $q=y$; $j=x$ when $u=l$ but $j=y$ when $u=h$. Equation (32) can be easily solved to obtain

$$P_u(z) = \frac{P_0 P_u(0)}{P_u(0) + P_v(0)\exp[g_\epsilon(\Omega_{uv}) P_0 z]}, \tag{33}$$

where $P_0 = P_l(z) + P_h(z)$ is the total input pump power that remains constant along the fiber, and ϵ denotes $\parallel$ and $\perp$ for parallel and orthogonal pumps, respectively.

As seen from Eq. (33), the two pumps transfer powers between them through stimulated Raman scattering (SRS). However, in a realistic experiment on photon-pair generation, the pump powers are maintained at a low level to prevent stimulated contribution. Under such conditions, $|g_\epsilon(\Omega_{hl}) P_0 L| \ll 1$, and the extent of SRS-induced pump power transfer is small. For an example of copolarized pumping, SRS only transfers 12% of the high-frequency pump power to the other one even when $\gamma P_0 L$ has a relatively large value of 0.5 and the second pump is located at the Raman gain peak ($|\Omega_{hl}|/2\pi = 13.2$ THz). In most cases, $\gamma P_0 L$ is smaller and pump frequency spacing is far from being 13.2 THz, resulting in negligible SRS-induced power transfer between the two pumps. For the case of orthogonal pumping, such Raman-induced power transfer is even much smaller [25]. Under such conditions, $\xi_q(\Omega_{uv}) \approx \xi_q(0)$ and $P_u(z) \approx P_u(0)$. The pump fields then evolve along the fiber as

$$A_{uj}(z) \approx A_u \exp\{iz[k_j(\omega_u) + \gamma P_u + \gamma \xi_q(0) P_v]\}, \tag{34}$$

where A_u is the input pump amplitude at ω_u.

Energy conservation during nondegenerate FWM requires $\omega_s + \omega_i = \omega_l + \omega_h$. From Eq. (6), the two polarization components of the signal are found to satisfy the following Heisenberg equation:

$$\frac{\partial \hat{A}_j(z,\omega_s)}{\partial z} = i[k_j(\omega_s) + \gamma \xi_j(\Omega_{sl}) P_l + \gamma \xi_q(\Omega_{sh}) P_h] \hat{A}_j(z,\omega_s) + i\gamma \eta_j(\omega_s) A_{lx} A_{h\sigma} \hat{A}_q^\dagger(z,\omega_i) + i A_{lx} \hat{m}_{jx}(z,\Omega_{sl}) + i A_{h\sigma} \hat{m}_{j\sigma}(z,\Omega_{sh}), \tag{35}$$

where j, $q=x$ or y and σ denotes the SOP of the high-frequency pump. For copolarized pumps, $q=j$ and $\sigma=x$. In contrast, $q \neq j$ and $\sigma=y$ for orthogonally polarized pumps. As before, the idler equation is obtained from Eq. (35) by interchanging subscripts s and i. In Eq. (35), $\eta_j(\omega_s) \equiv \eta_j(\Omega_{sl}) + \eta_j(\Omega_{sh})$ for the case of copolarized pumping, where $\eta_j(\Omega_{sl})$ and $\eta_j(\Omega_{sh})$ are given by either Eq. (12) or Eq. (13), depending on the signal SOP. In the case of orthogonal pumping, η_x and η_y are given by

$$\eta_x(\omega_s) = 2(1 - f_R)/3 + f_R \tilde{R}_a(\Omega_{sl}) + f_R \tilde{R}_b(\Omega_{sh})/2, \tag{36}$$

$$\eta_y(\omega_s) = 2(1 - f_R)/3 + f_R \tilde{R}_a(\Omega_{sh}) + f_R \tilde{R}_b(\Omega_{sl})/2. \tag{37}$$

In the case of orthogonal pumping, the FWM process can be decomposed into two "eigen" processes shown in Fig. 7. Equation (35) shows that the x-polarized signal only couples to the y-polarized idler and vice versa. Thus the two processes shown in Fig. 7 are independent of each other.

In both pumping configurations, the linear equation (35) provides an analytic solution similar to Eq. (14). It has the form

$$\hat{A}_j(L,\omega_s) = [\alpha_j(L,\omega_s) \hat{A}_j(0,\omega_s) + \beta_j(L,\omega_s) \hat{A}_q^\dagger(0,\omega_i) + \hat{N}_{lj}(L,\omega_s) + \hat{N}_{hj}(L,\omega_s)] \Phi(L), \tag{38}$$

where $q=j$ for copolarized pumping but $q \neq j$ for the orthogonal one. Explicit expressions for the coefficients α_j, β_j,

Φ, and noise operators $\hat{N}_{lj}$ and $\hat{N}_{hj}$ are given in Appendix A.

Another feature of the dual-pump configuration is that the two pumps introduce SpRS independently, as represented by the two noise operators in Eq. (38). We use Eq. (38) to investigate the photon statistics in the two pumping configurations. Detailed expressions of photon flux and pair correlation, including the contributions of both spontaneous and stimulated scattering, are given in Appendix B. In the following subsections, we focus on the case in which pump powers are low enough that spontaneous scattering dominates. To simplify the analysis, we also assume that narrow band signal and idler filters are located within the phase-matched spectral window such that $\bar{\omega}_s+\bar{\omega}_i=\omega_l+\omega_h$.

B. Photon flux and pair correlation: Copolarized pumping

One advantage of copolarized pumping is that the phase-matching condition can be satisfied over a broad spectral range when the two pumps are located on opposite sides of the zero-dispersion wavelength of the fiber and are separated far apart [48,51]. This configuration can provide a broad frequency range of available signal and idler photons with a nearly uniform photon-generation efficiency. In the general case shown in Fig. 6, the signal and idler frequencies are sandwiched between the two pumps because the phase-matching condition is easy to satisfy. In this case, the signal and the idler act simultaneously as the Stokes for the ω_h pump and the anti-Stokes for the ω_l pump. This situation leads to a significant impact on the photon-pair correlation.

In the case of two copolarized pumps, photon pairs can be created with polarization either parallel or orthogonal to the pumps, similar to the single-pump case discussed earlier. Comparing Eq. (38) with Eq. (14), we note that the two cases are quite similar. As a result, the discussion of Sec. III related to the polarization issues applies also to the copolarized dual-pump configuration. In the following, we focus on the photon pairs that are created copolarized with the pumps, and drop the polarization indices x and y for simplicity of notation.

Consider first the photon flux. In the low-power regime where $\gamma P_0 L \ll 1$, it is given by

$$I_u = \Delta\nu_u[|\gamma\eta_u L|^2 P_l P_h + P_l L|g_R(\bar{\Omega}_{ul})|\mathcal{N}_{ul} + P_h L|g_R(\bar{\Omega}_{uh})|\mathcal{N}_{uh}], \tag{39}$$

where $\eta_u=\eta(\bar{\Omega}_{ul})+\eta(\bar{\Omega}_{uh})$, $N_{uv}=\mathcal{N}(\bar{\Omega}_{uv})$, and $\bar{\Omega}_{uv}=\bar{\omega}_u-\omega_v$ with $v=l$ and h for the two pumps.

Different from the single-pump case, the FWM-created photon flux now depends on the product $P_l P_h$ of two pump powers, a quantity that is maximized when the two pumps have equal powers (for a constant total power). Moreover, both pumps introduce SpRS photons independently. In general, as the signal and idler have similar frequency relationships with each pump, SpRS generates a comparable number of noise photons for both waves. When the pump-signal frequency detuning is small (below 2 THz), the two pumps would create similar amounts of SpRS photons for the signal as well as the idler. When the frequency detuning increases, phonon population decreases and the contribution of the high-frequency pump dominates for both of them. This would increase the accidental coincidence counting and thus degrade the pair correlation.

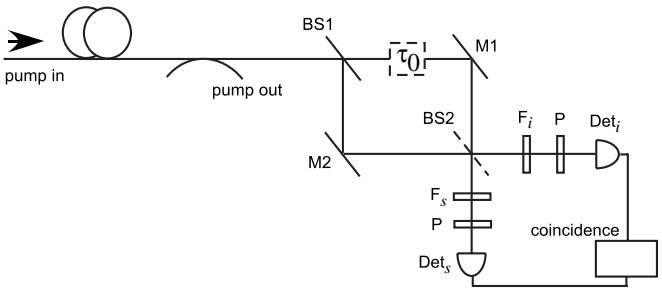

FIG. 8. Unbalanced Mach-Zehnder interferometer used for coincidence counting and for creating energy-time entanglement. BS: 50:50 beam splitter; M: mirror; P: polarizer; F_s and F_i: signal and idler filters; Det: photon-counting detector.

The degree of quantum correlation between the signal and idler photons can be obtained in a way similar to the case of single-pump configuration. Detailed expressions including both spontaneous and stimulated scattering are given in Appendix B. When the signal and idler are distinguishable on the basis of their frequencies [$\bar{\omega}_s \neq \bar{\omega}_i$, Fig. 6(a)], the pair correlation at a low pump level is given by

$$\rho_c(\tau) = |\varphi_c(\tau)|^2 P_l P_h (Y_1/Y_2), \tag{40}$$

where Y_1 and Y_2 are defined as

$$Y_1 = [\gamma\,\mathrm{Re}(\eta_s)]^2 + \left[|g_{Rl}|\left(n_l+\frac{1}{2}\right)+|g_{Rh}|\left(n_h+\frac{1}{2}\right)\right]^2, \tag{41}$$

$$Y_2 = [|\gamma\eta_s|^2 P_l P_h L + P_l|g_{Rl}|n_l + P_h|g_{Rh}|(n_h+1)] \times [|\gamma\eta_s|^2 P_l P_h L + P_l|g_{Rh}|n_h + P_h|g_{Rl}|(n_l+1)]. \tag{42}$$

Here, $g_{Ru}=g_R(\bar{\Omega}_{su})$ and $n_u=n(\bar{\Omega}_{su})$ with $u=l,h$. In the absence of SpRS, Eq. (40) reduces to a simple expression, $\rho_c(\tau)=|\varphi_c(\tau)|^2/(|\gamma\eta_s L|^2 P_l P_h)$. When the two pumps have equal powers, ρ_c has the same value as the single-pump configuration for a given total pump power (as $\eta_s=2$ in the absence of SpRS).

When the signal and idler photons are indistinguishable on the basis of their frequencies [$\bar{\omega}_s=\bar{\omega}_i$, Fig. 6(b)], coincidence counting can be realized through the experimental setup shown in Fig. 8 by removing the beam splitter BS2 and using identical filters for the two detectors [15]. As the two arms are identical, the pair correlation has the same form as in Eq. (23). In the case of low pump powers with $\gamma P_0 L \ll 1$, pair correlation is found to be

$$\rho_c(\tau) = |\varphi_s(\tau)|^2 + |\varphi_c(\tau)|^2 \times \frac{P_l P_h\{[\gamma\,\mathrm{Re}(\eta_s)]^2 + [|g_R|(2n+1)]^2\}}{[|\gamma\eta_s|^2 P_l P_h L + |g_R|(nP_0+P_h)]^2}, \tag{43}$$

where $g_R=g_R(\bar{\Omega}_{sl})$, $n=n(\bar{\Omega}_{sl})$, and we used $\bar{\Omega}_{sl}=\bar{\Omega}_{hs}$. Comparing Eq. (43) with Eq. (40), we find that the second term in Eq. (43) provides the cross correlation between the signal-

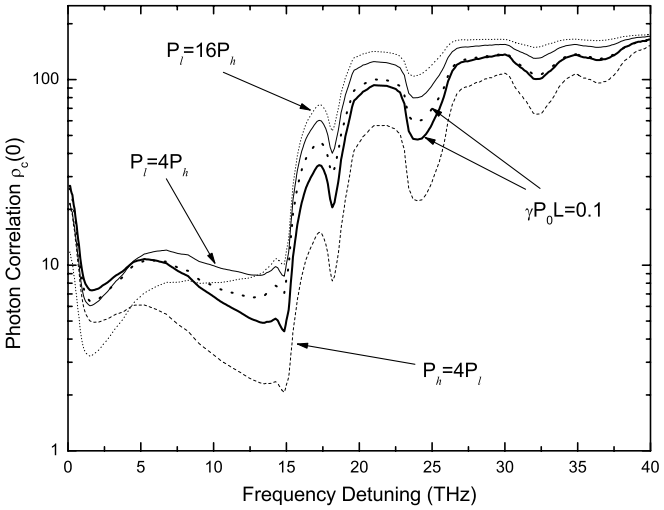

FIG. 9. Pair correlation $\rho_c(0)$ in the degenerate case shown in Fig. 6(b) for several power ratios of the two copolarized pumps. The dotted curve shows, for comparison, the single-pump case. In all cases, the FWM-generated flux is kept the same by choosing $P_0^2=4P_lP_h$.

idler photon pair. The first term reflects self-correlation of signal photons as spontaneous scattering enables creation of multiple pairs (although the probability is very small) that can pass through either arm and be detected by either of the two detectors (see Fig. 8).

The degenerate configuration shown in Fig. 6(b) can be thought of as the reverse process of that in Fig. 1(a) [15]. Figure 9 compares pair correlation in these two cases under the same FWM-generated photon rates by setting P_lP_h in Eq. (43) equal to $P_0^2/4$ and using $\gamma P_0 L=0.1$. In general, the two configurations exhibit a qualitatively similar behavior, especially at small frequency detunings (<4 THz) for which two pumps contribute almost equally to SpRS photons, and at very large frequency detunings (>27 THz) for which SpRS becomes negligible. However, the situation changes in the intermediate spectral range in which noise photons are dominantly introduced by the high-frequency pump. When the two pumps have equal powers (thick solid curves), $\rho_c(0)$ can be lower than the single-pump case (thick dotted curve) by 10 to 40% over a frequency range of 5–27 THz. Even though these two FWM processes act as the reverse of each other, they do not exhibit the same degree of correlation because of different SpRS processes involved. This difference is enhanced at low pump powers but decreases at high pump power levels for which FWM dominates.

As SpRS is dominated by the high-frequency pump over a quite broad spectral range, photon-pair correlation would strongly depend on the power imbalance between the two pumps. This is shown clearly in Fig. 9 where the FWM-generated photon rate is maintained constant. If P_h is four times larger than P_l (thin dashed curve), corresponding to a 1.25 times increase in total pump power, the correlation magnitude drops significantly (by 25 to 60%) over most of the detuning range, except in a small region below 1 THz. In contrast, the correlation can be enhanced by 20 to 100% if the pump powers are flipped such that $P_l=4P_h$ (thin solid curve). If we unbalance the pump powers further such that $P_l=16P_h$ (thin dotted curves), the correlation can be improved even more (by up to 140% compared with the equal-pump-power case) for detunings larger than 10 THz. However, it is degraded by a similar factor in the low-detuning region because of SpRS enhancement induced by an increase in the total pump power. These results show that the power imbalance between the two pumps may be used to advantage when a dual-pump configuration is adopted.

C. Photon flux and pair correlation: Orthogonal pumping

In this subsection, we consider the case of two linearly polarized pumps but orthogonal to each other, which allows, in principle, automatic generation of a polarization-entangled state. However, fiber birefringence usually makes the phase-matching conditions slightly different for the two eigenprocesses shown in Fig. 7, leading to partial distinguishability between them and degrading the degree of polarization entanglement. This situation is quite similar to the birefringence-induced distinguishability in a type-II $\chi^{(2)}$-based process [45]. Thus similar techniques can be used to engineer the indistinguishability [52]. Moreover, unlike nonlinear crystals, which generally exhibit a high intrinsic birefringence, silica glass is isotropic, and fiber birefringence mainly results from geometrical asymmetry or internal stress. Both of these can be reduced, in principle, to realize a low-birefringence fiber with a beat length longer than 10 m. As a result, birefringence effects can be mitigated to a negligible level if a high-nonlinearity fiber of length ~ 1 m is employed for photon-pair generation [15,16]. In the following discussion, we assume that the fiber is isotropic (no birefringence) and focus on the polarization effects of FWM and SpRS.

Although the two eigenprocesses have similar FWM efficiencies, they exhibit quite different polarization-dependent Raman scattering. In the process of Fig. 7(a), the signal and idler are copolarized with the low-frequency and high-frequency pumps, respectively. As a result, the signal is mainly coupled with the low-frequency pump, while the idler is mainly coupled with the high-frequency pump. The situation is reverse in Fig. 7(b). Such different Raman couplings are reflected through the polarization-dependent noise operators in Eq. (35); see Appendix A for detailed analytic expressions.

In general, a polarizer is placed in front of the detector to a select a specific polarization state of the incoming signal (or idler) photons. Assuming that the polarizer is aligned at an angle θ_u ($u=s,i$) with respect to the x axis of fiber, the optical field falling on the detector is given by

$$\hat{A}_u(t,\theta_u)=(\cos\theta_u)\hat{A}_{ux}(L,t)+(\sin\theta_u)\hat{A}_{uy}(L,t), \quad (44)$$

where $\hat{A}_{ux}(L,t)$ and $\hat{A}_{uy}(L,t)$ are x- and y-polarized signal or idler fields, respectively. As the two eigenprocesses shown in Fig. 7 are independent of each other, the photon flux is given by

$$I_u(\theta_u)=I_{ux}\cos^2\theta_u+I_{uy}\sin^2\theta_u, \quad (45)$$

where $I_{uj}\equiv\langle\hat{A}_{uj}^{\dagger}(L,t)\hat{A}_{uj}(L,t)\rangle$ is the photon flux for the jth polarization component ($j=x,y$) with $u=s$ and i. The general

expressions for I_{ux} and I_{uy} are given in Appendix B. When the pump powers are low enough that $\gamma P_0 L \ll 1$, they reduce to

$$I_{ux} = \Delta\nu_u[|\gamma\eta_{ux}L|^2 P_l P_h + P_l L|g_{\parallel}(\bar{\Omega}_{ul})|\mathcal{N}_{ul} + P_h L|g_{\perp}(\bar{\Omega}_{uh})|\mathcal{N}_{uh}], \quad (46)$$

$$I_{uy} = \Delta\nu_u[|\gamma\eta_{uy}L|^2 P_l P_h + P_l L|g_{\perp}(\bar{\Omega}_{ul})|\mathcal{N}_{ul} + P_h L|g_{\parallel}(\bar{\Omega}_{uh})|\mathcal{N}_{uh}], \quad (47)$$

where $\eta_{uj}=\eta_j(\bar{\omega}_u)$ $(u=s,i$ and $j=x,y)$ is given by Eqs. (36) and (37). If we compare these equations with Eq. (39), we find that, for the same pump power, the number of FWM-generated photons is about 1/9 of that in the copolarized-pump case, since η_{ux} and η_{uy} here are roughly 1/3 of η_u in Eq. (39). Moreover, these two equations show that, because of polarization dependence of Raman scattering, the two pumps provide different SpRS contributions to the two polarization components of the signal or idler. In general, SpRS photons are dominated by the copolarized pump, which is roughly half of the total pump power. Compared with the single-pump copolarized configuration [Fig. 1(a)], at the same pump level, the noise photon flux created by SpRS is reduced by a factor of 1/2, but the correlated one created by FWM is reduced by 1/9. Although this reduction in the latter can be simply compensated by increasing the total pump power by three times, it also enhances the former by a net factor of 1.5 compared with the single-pump case. Clearly, at a given FWM-generated photon rate, SpRS has a higher impact for this scheme than the single-pump one. As a result, pair correlation is expected to be degraded for the configuration of orthogonal pumping with linear pump SOPs.

For arbitrary polarization angles of the signal and idler waves, the pair correlation is found to have the form

$$\rho_c(\tau,\theta_s,\theta_i) = |\mathcal{P}_{xy}(\tau)\cos\theta_s \sin\theta_i + \mathcal{P}_{yx}(\tau)\sin\theta_s\cos\theta_i|^2/I_s(\theta_s)I_i(\theta_i), \quad (48)$$

where the quantities $\mathcal{P}_{xy}(\tau)\equiv\langle\hat{A}_{sx}(L,t+\tau)\hat{A}_{iy}(L,t)\rangle$ and $\mathcal{P}_{yx}(\tau)\equiv\langle\hat{A}_{sy}(L,t+\tau)\hat{A}_{ix}(L,t)\rangle$ are related to pair correlations in the two processes shown in Figs. 7(a) and 7(b), respectively. They are given by (see Appendix B for general expressions)

$$\mathcal{P}_{xy}(\tau) = \sqrt{\Delta\nu_s\Delta\nu_i}\varphi_c(\tau)A_l A_h L\left[i\gamma\,\mathrm{Re}(\eta_{sx}) - |g_{al}|\left(n_l+\frac{1}{2}\right) - |g_{\perp h}|\left(n_h+\frac{1}{2}\right)\right], \quad (49)$$

$$\mathcal{P}_{yx}(\tau) = \sqrt{\Delta\nu_s\Delta\nu_i}\varphi_c(\tau)A_l A_h L\left[i\gamma\,\mathrm{Re}(\eta_{sy}) - |g_{ah}|\left(n_h+\frac{1}{2}\right) - |g_{\perp l}|\left(n_l+\frac{1}{2}\right)\right], \quad (50)$$

where $g_{av}=g_a(\bar{\Omega}_{sv})$ and $g_{\perp v}=g_{\perp}(\bar{\Omega}_{sv})$ $(v=l,h)$. If we substitute Eqs. (49) and (50) into Eq. (48) and use Eqs. (46) and (47), we can obtain pair correlation for arbitrary combinations of signal and idler polarization angles.

In the absence of SpRS, $\eta_{sx}=\eta_{sy}=2/3$ and the preceding equations reduce to

$$\mathcal{P}_{xy}(\tau) = \mathcal{P}_{yx}(\tau) = 2i(\Delta\nu_s\Delta\nu_i)^{1/2}\varphi_c(\tau)\gamma A_l A_h L/3. \quad (51)$$

The two processes in Fig. 7 become indistinguishable from each other. The pair correlation in this specific case is given by

$$\rho_c(\tau,\theta_s,\theta_i) = \frac{9|\varphi_c(\tau)|^2\sin^2(\theta_s+\theta_i)}{4\gamma^2L^2P_lP_h}, \quad (52)$$

indicating a polarization-entangled Bell state of $(|H_s,V_i\rangle + |V_s,H_i\rangle)/2$, where H and V denote horizontal and vertical linear SOPs, respectively [3]. Accordingly, Eq. (52) has the maximal value of $\rho_c(\tau,0,\pi/2)=9|\varphi_c(\tau)|^2/(4\gamma^2L^2P_lP_h)$ for any orthogonal θ_s and θ_i.

As the biphoton probability of the signal-idler pair is given by $I_s(\theta_s)I_i(\theta_i)[1+\rho_c(\tau,\theta_s,\theta_i)]$, it varies with signal and idler polarization angles periodically. The resulting "fringe pattern" has a visibility of

$$V_f(\tau) = \frac{\rho_c(\tau,0,\pi/2)}{2+\rho_c(\tau,0,\pi/2)}. \quad (53)$$

Note that $V_f(0)$ is close to 1 when $\gamma P_0 L \ll 1$, indicating that FWM with two orthogonally polarized pumps can provide automatic polarization entanglement.

If the pump frequencies are close to each other, the two eigenprocesses in Fig. 7 would have almost the same values of pair correlation even in the presence of SpRS, since the signal and idler have similar frequency detunings from the two pumps. The visibility of biphoton probability is still given by Eq. (53) except that $\rho_c(\tau,0,\pi/2)$ is now provided by the general form in Eq. (48). Figure 10 compares the pair correlation for the process of Fig. 7(a) (curve *b*) with the single-pump configuration of Fig. 1(a) (curve *a*). The two pumps are assumed to have equal powers and their total power is three times larger than that of the single-pump case to maintain the same FWM-created photon flux. The pair correlation is significantly lower over a wide frequency range in the case of orthogonal pumping compared with the single-pump case because of an enhanced role played by SpRS in that case.

The situation is different when the two pumps are separated far apart with the signal and idler sandwiched in between. The signal (idler) is anti-Stokes (Stokes) of the low-frequency (high-frequency) pump with a frequency separation of $|\Omega_{sl}|$ in Fig. 11(a) but it is the Stokes (anti-Stokes) of the high-frequency (low-frequency) pump with a different frequency separation of $|\Omega_{sh}|$ in Fig. 11(b). As a result, the *x*-polarized signal or idler has fewer SpRS photons than the *y*-polarized one, leading to quite different pair correlations for the two processes of Figs. 11(a) and 11(b). The inset in Fig. 10 shows an example when the pump spacing is 1 THz. Not only is the pair correlation strongly polarization dependent, this polarization dependence increases with increased pump spacing.

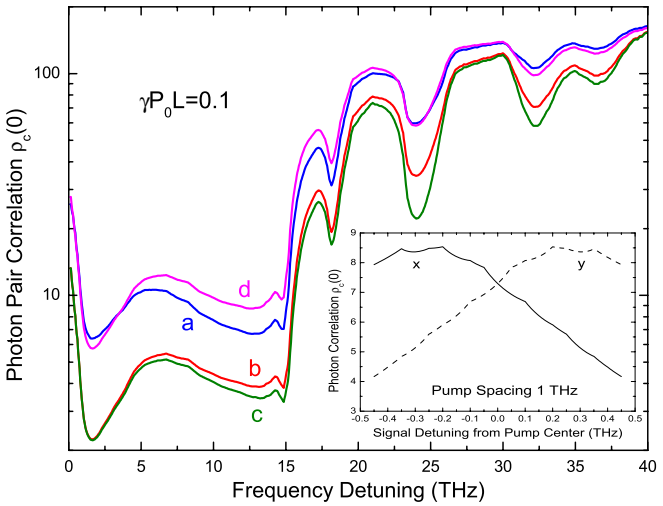

FIG. 10. (Color online) Comparison of pair correlation $\rho_c(0)$ in different pumping configurations. Curves *a* to *d* show the cases of Figs. 1(a), 7(a), 11(c), and 12, respectively. The inset shows the pair correlation for the two eigenprocesses of Figs. 11(a) and 11(b) with a fixed pump spacing of 1 THz. The total pump power is increased by a factor of 3 in the case of Figs. 7(a) and 11(c) and by 1.5 in Fig. 12 to maintain nearly the same FWM-created photon flux.

Such polarization dependence vanishes when the signal and idler frequencies are identical ($\bar{\omega}_s = \bar{\omega}_i$) and are located at the pump center [Fig. 11(c)]. In this case, photon self-correlation would generally contribute if the setup of Fig. 8 is employed for coincidence counting, similar to the copolarized dual-pump case discussed earlier. Equation (48) in this case changes to become

$$\rho_c'(\tau,\theta_s,\theta_i) = \rho_c(\tau,\theta_s,\theta_i) + \frac{|\varphi_s(\tau)|^2}{I_s(\theta_s)I_s(\theta_i)} \times |I_{sx}\cos\theta_s\cos\theta_i + I_{sy}\sin\theta_s\sin\theta_i|^2, \tag{54}$$

where ρ_c is given by Eq. (48). In general, the magnitude of the self-correlation term is less than 1, and the pair correlation is close to the case of Fig. 7. Curve *c* in Fig. 10 shows this case, in which the frequency detuning corresponds to half of the pump frequency spacing. Slightly lower values of the pair correlation are due to the enhancement of SpRS by

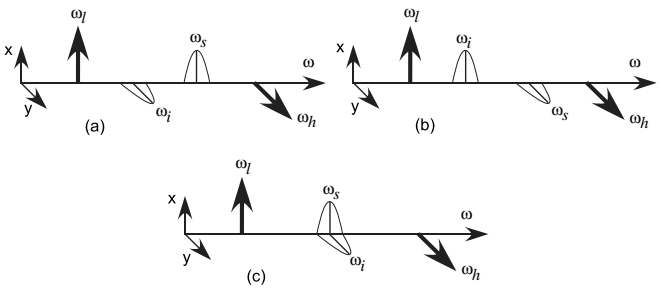

FIG. 11. Frequency and polarization relationships among the four waves in the case of two widely separated orthogonally polarized pumps.

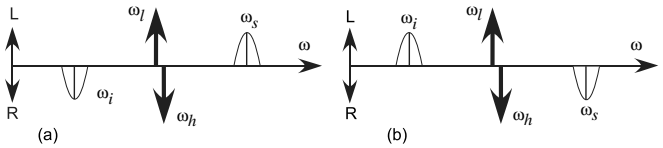

FIG. 12. Frequency and polarization relationships among the four waves in the case of two orthogonally circularly polarized pumps. *L* and *R* denote left- and right-circular polarizations, respectively.

the high-frequency pump. Similar to the case of copolarized pumping, imbalance of pump powers can be used to improve the performance of photon pair generation in this case when the two pumps are separated far apart. However, it cannot be used for the case of Fig. 7 when the two pumps are located closely and sandwiched between the signal and idler, as where the idler at the Stokes is copolarized with either of the two pumps, depending on its SOP.

D. Orthogonal pumping with circular polarizations

The previous subsection shows that, although orthogonal pumps with linear SOPs can automatically generate polarization-entangled photon pairs, such a scheme suffers from a significant reduction in FWM efficiency, which leads to a degraded photon pair quality. This problem can be solved if the two pumps are chosen to have circular SOPs that are orthogonal to each other, a configuration with the maximum FWM efficiency among all orthogonal pumping schemes [51]. In this subsection, we show that this scheme can also generate photon pairs in a polarization-entangled state, while maintaining relatively high pair correlation. We assume the fiber to be isotropic (no birefringence) and focus on the polarization effects of FWM and SpRS.

It is convenient to discuss this process in a basis in which $\uparrow$ and $\downarrow$ denote the left and right circular polarization states, carrying an intrinsic spin of $+\hbar$ (spin up) and $-\hbar$ (spin down), respectively [39]. The polarization components in this basis are related to those in a basis of linear polarization as $\hat{A}_\uparrow = (\hat{A}_x + i\hat{A}_y)/\sqrt{2}$ and $\hat{A}_\downarrow = (\hat{A}_x - i\hat{A}_y)/\sqrt{2}$. Assuming that the low- and high-frequency pumps are left- and right-circularly polarized, respectively (Fig. 12), we find that the pump fields satisfy an equation similar to Eq. (32):

$$\frac{\partial A_{uj}}{\partial z} = i[k(\omega_u) + \gamma\xi_0(0)P_u + \gamma\xi_\downarrow(\Omega_{uv})P_v]A_{uj}, \tag{55}$$

where $u \neq v$, $j = \uparrow$ when $u = l$ but $j = \downarrow$ when $u = h$. $\xi_0(\Omega)$ and $\xi_\downarrow(\Omega)$ are given by

$$\xi_0(\Omega) = 2(1 - f_R)/3 + f_R\tilde{R}_a(\Omega) + f_R\tilde{R}_b(\Omega)/2, \tag{56}$$

$$\xi_\downarrow(\Omega) = 4(1 - f_R)/3 + f_R\tilde{R}_b(\Omega) + f_R\tilde{R}_a(0) + f_R\tilde{R}_b(0)/2. \tag{57}$$

It is easy to show from Eq. (55) that SRS-induced pump power transfer is negligible, similar to the previous orthogonal pumping scheme with linear pump SOPs.

It turns out that, because of a spin selection rule among the four interacting photons, FWM process can be decoupled into two eigenprocesses shown in Fig. 12, where $\uparrow_l+\downarrow_h \rightarrow \uparrow_s+\downarrow_i$ in (a), and $\uparrow_l+\downarrow_h \rightarrow \downarrow_s+\uparrow_i$ in (b). If we decompose optical fields into the basis of circular polarization, from Eq. (6), the two polarization components of the signal are found to satisfy the following Heisenberg equation:

$$\frac{\partial \hat{A}_j(z,\omega_s)}{\partial z} = i[k(\omega_s) + \gamma\xi_j(\Omega_{sl})P_l + \gamma\xi_q(\Omega_{sh})P_h]\hat{A}_j(z,\omega_s) + i\gamma\eta_j(\omega_s)A_{l\uparrow}A_{h\downarrow}\hat{A}_q^{\dagger}(z,\omega_i) + iA_{l\uparrow}\hat{m}_{j\uparrow}(z,\Omega_{sl}) + iA_{h\downarrow}\hat{m}_{j\downarrow}(z,\Omega_{sh}), \quad (58)$$

where $j,q=\uparrow$ or $\downarrow$ $(q\neq j)$, $\xi_{\uparrow}(\Omega)=\xi_0(0)+\xi_0(\Omega)$, and the two quantities governing the FWM efficiency, $\eta_{\uparrow}$ and $\eta_{\downarrow}$, are given by

$$\eta_{\uparrow}(\omega_s) = 4(1-f_R)/3 + f_R\tilde{R}_b(\Omega_{sh}) + f_R\tilde{R}_a(\Omega_{sl}) + f_R\tilde{R}_b(\Omega_{sl})/2, \quad (59)$$

$$\eta_{\downarrow}(\omega_s) = 4(1-f_R)/3 + f_R\tilde{R}_b(\Omega_{sl}) + f_R\tilde{R}_a(\Omega_{sh}) + f_R\tilde{R}_b(\Omega_{sh})/2. \quad (60)$$

The noise operators $\hat{m}_{jq}$ $(j,q=\uparrow,\downarrow)$ in Eq. (58) are related to those in the basis of linear polarizations in Eq. (8). Their detailed expressions are given in Appendix C. The idler equation is obtained from Eq. (58) by interchanging subscripts s and i.

As Eq. (58) is quite similar to Eq. (35), it has a solution similar to Eq. (38) except that the subscript x and y are replaced by $\uparrow$ and $\downarrow$, respectively, and that ξ and η in all coefficients are changed accordingly (see Appendix C for the field solution). Using this solution, we obtain the generated photon flux of the two waves. For a linearly polarized field given in Eq. (44), the photon flux is found to be given by a simple form independent of its polarization angle:

$$I_u(\theta_u) = (I_{u\uparrow} + I_{u\downarrow})/2, \quad (61)$$

where $u=s,i$ and $I_{uj}\equiv\langle\hat{A}_{uj}^{\dagger}(L,t)\hat{A}_{uj}(L,t)\rangle$ is the photon flux for the left $(j=\uparrow)$ and right $(j=\downarrow)$ circularly polarized components, respectively. In the low-pump-power limit of $\gamma P_0 L \ll 1$, fluxes are given by

$$I_{u\uparrow} = \Delta\nu_u\{|\gamma\eta_{u\uparrow}L|^2P_lP_h + P_hL\mathcal{N}_{uh}|g_b(\bar{\Omega}_{uh})| + P_lL\mathcal{N}_{ul}[|g_a(\bar{\Omega}_{ul})| + |g_b(\bar{\Omega}_{ul})|/2]\}, \quad (62)$$

$$I_{u\downarrow} = \Delta\nu_u\{|\gamma\eta_{u\downarrow}L|^2P_lP_h + P_lL\mathcal{N}_{ul}|g_b(\bar{\Omega}_{ul})| + P_hL\mathcal{N}_{uh}[|g_a(\bar{\Omega}_{uh})| + |g_b(\bar{\Omega}_{uh})|/2]\}, \quad (63)$$

where $\eta_{uj}=\eta_j(\bar{\omega}_u)$ $(u=s,i$ and $j=\uparrow,\downarrow)$ is given by Eqs. (59) and (60). Comparing these two equations with Eqs. (46) and (47), we see that, for the same pump power, FWM-generated photon flux is increased by four times while the number of SpRS created noise photons remains nearly the same, as $\eta_{u\uparrow}$ and $\eta_{u\downarrow}$ here are roughly twice as large as η_{ux} and η_{uy} in Eqs. (46) and (47), and as SpRS is still dominated only by the copolarized pump. As a result, the ratio of true coincidental counting over the accidental one would be enhanced considerably, leading to a much higher value of pair correlation. This scheme, compared with the single-pump scheme of Fig. 1(a), requires a 1.5 time total pump power to obtain a given FWM-created photon flux, but only half of the power contributes to SpRS, resulting in a net reduction of SpRS by about 25%. Clearly, this scheme would have a pair correlation higher than the single-pump scheme of Fig. 1(a).

For linearly polarized signal and idler [Eq. (44)], the pair correlation is found to have the form

$$\rho_c(\tau,\theta_s,\theta_i) = |\mathcal{P}_{\uparrow\downarrow}(\tau)e^{-i\Delta\theta_{si}} + \mathcal{P}_{\downarrow\uparrow}(\tau)e^{i\Delta\theta_{si}}|^2/(4I_sI_i), \quad (64)$$

where $\Delta\theta_{si}=\theta_s-\theta_i$, and we have dropped the angle arguments for I_s and I_i because of their independence on the polarization angle [Eq. (61)]. $\mathcal{P}_{\uparrow\downarrow}(\tau)\equiv\langle\hat{A}_{s\uparrow}(L,t+\tau)\hat{A}_{i\downarrow}(L,t)\rangle$ and $\mathcal{P}_{\downarrow\uparrow}(\tau)\equiv\langle\hat{A}_{s\downarrow}(L,t+\tau)\hat{A}_{i\uparrow}(L,t)\rangle$ are related to pair correlations for the two eigenprocesses shown in Figs. 12(a) and 12(b), respectively. At a low pump level with $\gamma P_0 L\ll 1$, they are found to be

$$\mathcal{P}_{\uparrow\downarrow}(\tau) = \sqrt{\Delta\nu_s\Delta\nu_i}\varphi_c(\tau)A_lA_hL \times\{i\gamma\eta_{s\uparrow} - \mathcal{N}_{sl}[|g_a(\bar{\Omega}_{sl}) + g_b(\bar{\Omega}_{sl})/2|]\}, \quad (65)$$

$$\mathcal{P}_{\downarrow\uparrow}(\tau) = \sqrt{\Delta\nu_s\Delta\nu_i}\varphi_c(\tau)A_lA_hL \times\{i\gamma\eta_{s\downarrow} - \mathcal{N}_{sh}[|g_a(\bar{\Omega}_{sh}) + g_b(\bar{\Omega}_{sh})/2|]\}. \quad (66)$$

In the absence of SpRS, $\eta_{s\uparrow}=\eta_{s\downarrow}=4/3$ and Eqs. (65) and (66) become $\mathcal{P}_{\uparrow\downarrow}(\tau)=\mathcal{P}_{\downarrow\uparrow}(\tau)$, which has the form of Eq. (51) except that the factor of 2 is replaced by 4. The pair correlation is thus given by a simple form of

$$\rho_c(\tau,\theta_s,\theta_i) = \frac{9|\varphi_c(\tau)|^2\cos^2(\theta_s-\theta_i)}{16\gamma^2L^2P_lP_h}, \quad (67)$$

which indicates a polarization-entangled Bell state of $(|H_s,H_i\rangle+|V_s,V_i\rangle)/2$ [3]. It has a maximum correlation value whenever the linear SOPs of the signal and idler are parallel to each other $(\theta_s=\theta_i)$.

In the presence of SpRS, the general expressions of Eqs. (62)–(66) should be used to find the photon pair correlation. Curve d of Fig. 10 shows an example with polarization angles of $\theta_s=\theta_i=0$. Comparing it with curve b for the orthogonal pumps with linear SOPs, we find that pair correlation is significantly enhanced by more than 100% over most of the spectrum. This scheme has a pair correlation even slightly higher than that for the single-pump case of Fig. 1(a) (curve a). Clearly, this scheme exhibits a great advantage for creating polarization-entangled photon pairs with high quality but without the complicated experimental configuration required for the time-multiplexing [19] or polarization diversity scheme [18].

In practice, self- and cross-phase modulations from the pumps introduce nonlinear polarization rotations which may perturb the circular SOPs of the pumps [51]. However, such rotations are negligible here because the pump powers used

for creating correlated photon pairs are relatively small. On the other hand, linear fiber birefringence can also cause the pump SOPs to deviate from the circular polarization. However, this perturbation can be mitigated to a small level as long as the fiber length is much less than the beat length. As discussed in the previous subsection, this is possible since high-nonlinearity fiber with a length of ~1 m is enough for creating photon pairs with high brightness [12,15,16], and current technology enables manufacturing fibers with a beat length longer than 10 m. Therefore, we expect that this scheme would become a simple but efficient technique for generating polarization-entangled photon pairs of high quality.

V. IMPACT ON QUANTUM ENTANGLEMENT

The degradation of photon correlation induced by SpRS would directly impact any quantum entanglement constructed from the photon pairs created through FWM inside an optical fiber. Here, we consider two examples and study how SpRS affects the energy-time and polarization entanglement.

A. Energy-time entanglement

The energy-time entanglement [1] can be realized with an unbalanced Mach-Zehnder interferometer [53–55] made by inserting the beam splitter BS2 as shown in Fig. 8 schematically. The relative time delay in the two arms should be much larger than the coherence time of signal or idler photons (to prevent first-order interference) but much shorter than the pump coherence time (to maintain time indistinguishability) [56]. The equal-time biphoton probability between the two outputs, $p_{12} \equiv \langle \hat{A}_1^\dagger(t)\hat{A}_2^\dagger(t)\hat{A}_2(t)\hat{A}_1(t)\rangle$, is found to be

$$p_{12} = \frac{I_s I_i}{4}\left\{1 + \frac{1}{2}\rho_c(0)[1 - \cos(2\omega_p\tau_0 + 2\phi_0)]\right\}, \quad (68)$$

where τ_0 and ϕ_0 are time and phase delay between the two arms. The subscripts 1 and 2 denote the two output ports of the Mach-Zehnder interferometer. The fringe visibility of two-photon quantum interference is thus given by

$$V_f = \frac{\rho_c(0)}{2 + \rho_c(0)}. \quad (69)$$

Quantum entanglement requires $\rho_c(0) \gg 2$ so that it can be clearly distinguished from the classical visibility of 50% [57,58]. A higher value of pair correlation translates into a higher degree of entanglement. Any reduction in the correlation induced by SpRS would directly deteriorate the degree of entanglement. For example, a typical correlation value of 10 obtained experimentally would result in a fringe visibility of only 83%. In practice, $\rho_c(0)$ values of 20 or more are desirable to realize a visibility of quantum interference >90%.

B. Polarization entanglement

A polarization-entangled state can be constructed by degenerate FWM through time multiplexing [19] or a polarization diversity scheme [18]. As we mentioned earlier, such a state can also be created automatically through nondegenerate FWM with orthogonal pumping. The degree of quantum entanglement can be tested by the extent of its violation to the Clauser, Horne, Shimony, and Holt (CHSH) inequality, $|S(\tau)| \leqslant 2$, where the CHSH parameter $S(\tau)$ is defined as [59,60]

$$S(\tau) = E(\tau, \theta_s, \theta_i) - E(\tau, \theta_s, \theta_i') + E(\tau, \theta_s', \theta_i) + E(\tau, \theta_s', \theta_i'). \quad (70)$$

Here, $E(\tau, \theta_s, \theta_i)$ is a correlation function defined as $E(\tau, \theta_s, \theta_i) = \mathcal{E}_-(\tau)/\mathcal{E}_+(\tau)$, where $\mathcal{E}_\pm(\tau) \equiv \langle \mathcal{T}{:}\hat{I}_{s\pm}(t+\tau)\hat{I}_{i\pm}(t){:}\rangle$, :: denotes normal ordering, and $\mathcal{T}$ denotes time ordering. $\hat{I}_{u\pm}(t)$ is the sum and difference photon-flux operator for two orthogonal polarization angles of θ_u $(u=s,i)$ and $\theta_{u\perp} = \theta_u + \pi/2$. It is defined as

$$\hat{I}_{u\pm}(t) \equiv \hat{A}_u^\dagger(t, \theta_u)\hat{A}_u(t, \theta_u) \pm \hat{A}_u^\dagger(t, \theta_{u\perp})\hat{A}_u(t, \theta_{u\perp}), \quad (71)$$

where $\hat{A}_u(t, \theta_u)$ and $\hat{A}_u(t, \theta_{u\perp})$ are given by Eq. (44) with polarization angle θ_u and $\theta_{u\perp}$, respectively. It is easy to show that $\hat{I}_{u+}(t)$ is invariant with the polarization angle because it represents the total photon flux.

In practice, the CHSH parameter requires sixteen measurements of coincidence counting between signal and idler performed with all possible combinations of angles θ_s, θ_s', θ_i, θ_i', and four angles orthogonal to them [3]. Although Eq. (70) looks complicated, it turns out that the CHSH parameter can be written in a compact form in a circular-polarization basis as

$$S(\tau) = \frac{1}{\mathcal{E}_+(\tau)}[\Gamma_1(\tau)\Theta_1 + \Gamma_2(\tau)\Theta_2 + \text{c.c.}], \quad (72)$$

where c.c. denotes complex conjugate, and $\Gamma_1(\tau)$ and $\Gamma_2(\tau)$ are given by

$$\Gamma_1(\tau) = \langle \hat{A}_{i\uparrow}^\dagger(t)\hat{A}_{s\uparrow}^\dagger(t+\tau)\hat{A}_{s\downarrow}(t+\tau)\hat{A}_{i\downarrow}(t)\rangle, \quad (73)$$

$$\Gamma_2(\tau) = \langle \hat{A}_{i\downarrow}^\dagger(t)\hat{A}_{s\uparrow}^\dagger(t+\tau)\hat{A}_{s\downarrow}(t+\tau)\hat{A}_{i\uparrow}(t)\rangle. \quad (74)$$

Here, $\hat{A}_{u\uparrow}$ and $\hat{A}_{u\downarrow}$ $(u=s,i)$ denote the field operators for left- (spin-up) and right-circular (spin-down) polarizations, respectively. They are related to the linearly polarized components as $\hat{A}_{u\uparrow} = (\hat{A}_{ux} + i\hat{A}_{uy})/\sqrt{2}$ and $\hat{A}_{u\downarrow} = (\hat{A}_{ux} - i\hat{A}_{uy})/\sqrt{2}$. In Eq. (72), the factors Θ_1 and Θ_2 are related to various polarization angles as

$$\Theta_1 = e^{2i(\theta_s+\theta_i)} - e^{2i(\theta_s+\theta_i')} + e^{2i(\theta_s'+\theta_i)} + e^{2i(\theta_s'+\theta_i')}, \quad (75)$$

$$\Theta_2 = e^{2i(\theta_s-\theta_i)} - e^{2i(\theta_s-\theta_i')} + e^{2i(\theta_s'-\theta_i)} + e^{2i(\theta_s'-\theta_i')}. \quad (76)$$

In the following subsections, we use Eqs. (72)–(76) to find $S(\tau)$ for the polarization-entangled states constructed from different FWM processes, and use it to discuss the impact of SpRS.

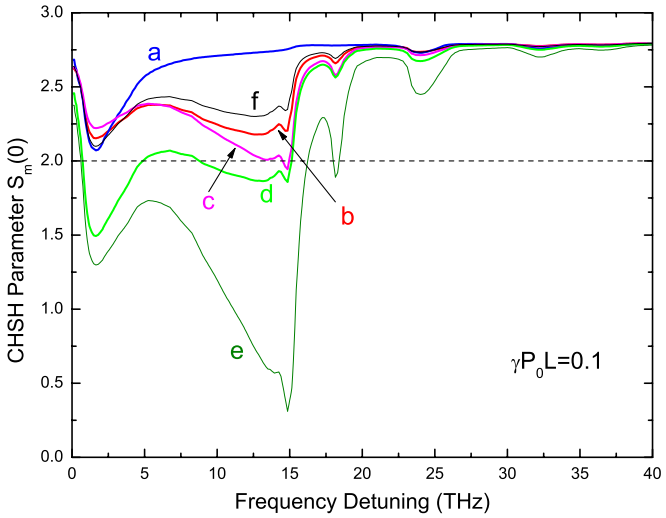

FIG. 13. (Color online) Comparison of CHSH parameter for different FWM configurations at a pump level of $\gamma P_0 L=0.1$. Curves *a* to *f* correspond to FWM configurations shown in Figs. 1(b), 1(a), 6(b), 7, 11(c), and 12. In the cases *a*–*c*, orthogonally polarized noise background is assumed to be removed. The two pumps have equal powers in the dual-pump cases. In the cases of orthogonal pumping, the total pump power is adjusted accordingly to maintain a nearly same FMW-created photon flux, similar to Fig. 10.

1. Degenerate FWM with a single pump

Although each photon pair created through degenerate FWM is copolarized (Fig. 1), a polarization-entangled state can be constructed by employing a time-multiplexing technique [19] or a polarization diversity loop [18]. The pump is split into two parts of equal powers with orthogonal polarizations, each part generating independent photon pairs with half probability. After combining them together and erasing the time or path information between them, a polarization-entangled state is constructed.

For such polarization-entangled states, we are able to find an analytic expression for the maximal value of the CHSH parameter $S_m(\tau)$ (see Appendix D). When the pump power is split equally between two paths, it takes the following simple form:

$$S_m(\tau) = \frac{2\sqrt{2}\rho_c(\tau)}{2+\rho_c(\tau)}. \tag{77}$$

This equation shows that the CHSH inequality is violated for $\rho_c(\tau) > 2/(\sqrt{2}-1) \approx 4.8$. If photon-pair generation is dominated by FWM with $\rho_c(0) \gg 5$, $S_m(0) \to 2\sqrt{2}$, indicating a clear violation of the CHSH inequality. A typical experimental value of $\rho_c(0)=10$ corresponds to $S_m(0)=2.36$. The same conclusions apply to the case of copolarized dual pumping (Fig. 6), as the two cases are quite similar. In the case of Fig. 6(b), photon self-correlation would contribute to coincidence counting and $\rho_c(\tau)$ given in Eq. (43) should be used.

Figure 13 show the CHSH parameter in different pumping configurations. In general, the orthogonal FWM in the single-pump configuration [Fig. 1(b)] (curve *a*) has the largest $S_m(0)$ value, indicating the best performance. In particular, it exhibits $S_m(0)$ values close to the maximum value of $2\sqrt{2}$ over a wide range of frequency detuning. In the copolarized FWM of single-pump configuration [Fig. 1(a)] (curve *b*), SpRS degrades the value of $S_m(0)$ significantly over a broad spectral range of 2–15 THz. The situation becomes worse for the copolarized FWM of dual-pump configuration [Fig. 6(b)] (curve *c*) because of the dominant SpRS induced by the high-frequency pump.

In general, the pump not only creates correlated copolarized signal-idler pairs but also generates an orthogonally polarized noise background through anisotropic Raman scattering. If such orthogonally polarized noise is not filtered out, it would contribute to photon fluxes of the signal and idler and would introduce extra accidental coincidence counting. In this case, Eq. (77) is still valid if $\rho_c(\tau)$ is given as the realistic ratio between the true coincidence counting and accidental one. It is interesting to note that the polarization diversity loop can automatically remove such orthogonally polarized noise background.

2. Nondegenerate FWM with orthogonally polarized pumps

We consider first the case of orthogonal pumping with linear SOPs. When the signal and idler are distinguishable [$\bar{\omega}_s \neq \bar{\omega}_i$, Fig. 7, or Figs. 11(a) and 11(b)], the maximum CHSH parameter is found to be (see Appendix D)

$$S_m(\tau) = \frac{\sqrt{2}[|\mathcal{P}_{xy}(\tau)+\mathcal{P}_{yx}(\tau)|^2 - \Delta I_s \Delta I_i]}{I_{s+}I_{i+} + |\mathcal{P}_{xy}(\tau)|^2 + |\mathcal{P}_{yx}(\tau)|^2}, \tag{78}$$

where $\Delta I_u \equiv I_{ux} - I_{uy}$ and $I_{u+} \equiv I_{ux} + I_{uy}$ $(u=s,i)$ are difference and sum photon flux of two polarization components. As the magnitudes of $\mathcal{P}_{xy}(\tau)$ and $\mathcal{P}_{yx}(\tau)$ are directly related to the magnitude of pair correlation, a higher correlation value implies a larger value of $|S_m(\tau)|$. In the absence of SpRS, Eq. (78) reduces to Eq. (77) with $\rho_c(\tau)=\rho_c(\tau,0,\pi/2) = 9|\varphi_c(\tau)|^2/(4\gamma^2 L^2 P_l P_h)$. Clearly, $|S_m(\tau)| \to 2\sqrt{2}$ when $\gamma L\sqrt{P_l P_h} \ll 1$. Thus, FWM-generated photon pairs at low power levels would exhibit a high degree of polarization entanglement.

Unfortunately, SpRS considerably increases the accidental counting rate [first term in the denominator of Eq. (78)], and thus reduces the magnitude of $|S_m(\tau)|$. In particular, when the two pump frequencies are close to each other, the two processes of Fig. 7 experience similar SpRS, and Eq. (78) again reduces to Eq. (77), except that $\rho_c(\tau)=\rho_c(\tau,0,\pi/2)$ is now provided by the general form of Eq. (48). Curve *d* of Fig. 13 shows the CHSH parameter for this case (Fig. 7). It has a value significantly lower than that of copolarized configuration, particularly in the low-frequency regime. Even for such a low pump level of $\gamma P_0 L=0.1$, it is difficult to violate the CHSH inequality for a broad spectral range from 1 to 15 THz.

When the signal and idler are indistinguishable [$\bar{\omega}_s = \bar{\omega}_i$, Fig. 11(c)], photon self-correlation starts to contribute because the polarization-angle settings for coincidence counting are generally not orthogonal to each other. In this case, the CHSH parameter is found to be (see Appendix D)

$$S_m(\tau) = \frac{\sqrt{2}[4I_{sx}I_{sy}\rho_c(\tau) - (\Delta I_s)^2(1+|\varphi_s(\tau)|^2)]}{I_{s+}^2 + |\varphi_s(\tau)|^2(I_{sx}^2 + I_{sy}^2) + 2I_{sx}I_{sy}\rho_c(\tau)}, \quad (79)$$

where $\rho_c(\tau)=\rho_c(\tau,0,\pi/2)$ is given by Eq. (48). For a pure FWM process without SpRS, indistinguishability between the two eigenprocesses reduces Eq. (79) to a simple form of

$$S_m(\tau) = \frac{2\sqrt{2}\rho_c(\tau)}{2+|\varphi_s(\tau)|^2 + \rho_c(\tau)}, \quad (80)$$

where $\rho_c(\tau)=9|\varphi_c(\tau)|^2/(4\gamma^2L^2P_lP_h)$. The appearance of $\varphi_s(\tau)$ in Eqs. (79) and (80) is an indication of the involvement of photon self-correlation, which is due to the collinear nature of FWM in optical fibers. Equations (79) and (80) show that photon self-correlation increases the requirement of pair correlation for violation of the CHSH inequality. For example, Eq. (80) shows that $|S_m(0)|>2$ requires $\rho_c(0)>7.2$. Moreover, Eq. (79) shows that polarization-dependent SpRS introduces different noise photons to the x- and y-polarized signals and thus degrades the magnitude of $S_m(\tau)$ even more. This can be seen by curve e of Fig. 13. It is much lower than any other cases over a broad spectral range. It is even much lower than 2 in the region 1–17 THz, indicating the impossibility of violation of the CHSH inequality. However, if the photon pairs have high quality with large pair correlation $[\rho_c(\tau) \gg |\varphi_s(\tau)|^2 < 1]$, photon self-correlation would have negligible effect on the CHSH inequality, as can be seen in curve e when frequency detuning is beyond 20 THz.

In the case of orthogonal pumping with circular SOPs (Fig. 12), the maximum CHSH parameter is found to have the form (see Appendix D)

$$S_m(\tau) = \frac{\sqrt{2}[\mathcal{P}_{\uparrow\downarrow}^*(\tau)\mathcal{P}_{\downarrow\uparrow}(\tau) + \mathcal{P}_{\uparrow\downarrow}(\tau)\mathcal{P}_{\downarrow\uparrow}^*(\tau)]}{I_{s+}I_{i+} + |\mathcal{P}_{\uparrow\downarrow}(\tau)|^2 + |\mathcal{P}_{\downarrow\uparrow}(\tau)|^2}, \quad (81)$$

where $I_{u+} \equiv I_{u\uparrow} + I_{u\downarrow}$ $(u=s,i)$. Similar to the case of orthogonal pumping with linear SOPs, for the process shown in Fig. 12 where the process (a) and (b) have a similar frequency relationship with the two closely located pumps, Eq. (81) reduces to the simple form of Eq. (77) with $\rho_c(\tau)=\rho_c(\tau,0,0)$ given by Eq. (64). Curve f of Fig. 13 shows $S_m(0)$ for this case. In general, it has a value well above 2, showing a clear violation of CHSH inequality over the whole spectrum at this pump level. It has a value of $S_m(0)$ not only much higher than any other dual-pump configuration, but also higher than that constructed from the copolarized FWM in the single-pump configuration [Fig. 1(a)]. Moreover, this scheme does not need complex experimental configurations as those required for the time-multiplexing [19] or polarization diversity scheme [18]. Therefore, it is promising for creating fiber-based polarization-entangled photon pairs with a high quality.

VI. SUMMARY

In summary, we have developed a general quantum theory capable of describing photon statistics under the combined effects of FWM and Raman scattering inside optical fibers. Our theory is vectorial in nature and includes all polarization effects. We have applied our general formalism to investigate photon-pair generation in various typical pumping configurations. When a single pump wave is launched into a fiber, it is possible to create the photon pairs with polarization either parallel or orthogonal to the pump. Our results show that the orthogonal configuration can improve the magnitude of pair correlation considerably over a broad spectrum. The reason for the improvement is related to the fact that Raman gain almost vanishes for an orthogonally polarized pump.

A dual-pump configuration can provide more quantum functionalities because of freedom to control pump parameters like frequencies, polarizations, powers, etc. When two pumps are copolarized, it is desirable to create photon pairs whose frequencies lie in between the two pumps because it is easy to satisfy the phase-matching condition. It is also possible to create photon pairs with the same frequency. Our results show that the quality of created photon pairs can be improved by optimizing the imbalance between the two pump powers. When two pumps are orthogonally polarized, we show that FWM can generate photon pairs automatically in a polarization-entangled state. Our results show that SpRS has significant impact when the two pump polarizations are linear because FWM efficiency is considerably reduced compared with SpRS, and because FWM has different polarization dependence from SpRS. However, such degradations can be significantly mitigated if two pumps have orthogonal circular polarizations. In this case, one can generate a polarization-entangled state with high quality but without a complicated experiment configuration required for time-multiplexing and polarization diversity schemes.

ACKNOWLEDGMENTS

The authors thank J. H. Eberly, M. N. O'Sullivan-Hale, I. A. Khan, and S. Radic for helpful discussions. This work is supported by the National Science Foundation under Grants Nos. ECS-0320816 and ECS-0334982.

APPENDIX A: FIELD SOLUTIONS IN DUAL-PUMP CONFIGURATION

In the case of dual pumping with linear pump SOPs, α_j and β_j $(j=x,y)$ in Eq. (38) are still given by Eqs. (15) and (16) except that A_p^2 is replaced by A_lA_h and η_j changes according to the pump SOP. $\eta_j(\omega_s)=\eta_j(\Omega_{sl})+\eta_j(\Omega_{sh})$ for copolarized pumps, where $\eta_j(\Omega_{sl})$ and $\eta_j(\Omega_{sh})$ are given by either Eq. (12) or Eq. (13). But η_j is given in Eqs. (36) and (37) for orthogonal pumping. The other parameters are given by

$$g_j^2 = (\gamma\eta_j)^2P_lP_h - (\kappa_j/2)^2, \quad (A1)$$

$$\kappa_j = k_j(\omega_s) + k_q(\omega_i) - k_x(\omega_l) - k_\sigma(\omega_h) + \gamma P_0[\xi_j(\Omega_{sl}) + \xi_q(\Omega_{sh}) - \xi_q(0) - 1]. \quad (A2)$$

$$K_j = \frac{1}{2}\{k_j(\omega_s) - k_q(\omega_i) + \gamma(P_l - P_h)[\xi_j(\Omega_{sl}) - \xi_q(\Omega_{sh})]\}. \quad (A3)$$

$$\Phi(L) = \exp\left\{\frac{i}{2}L\{k_x(\omega_l) + k_\sigma(\omega_h) + \gamma P_0[1 + \xi_q(0)]\}\right\}. \tag{A4}$$

The accumulated noise operators in Eq. (38) are found to be

$$\hat{N}_{lj}(L,\omega_s) = i\int_0^L \{A_l\alpha_j(L-z,\omega_s)\hat{m}_{jx}(z,\Omega_{sl}) - A_h^*\beta_j(L-z,\omega_s)\hat{m}_{q\sigma}(z,\Omega_{sl})\}e^{i\Delta z}dz, \tag{A5}$$

$$\hat{N}_{hj}(L,\omega_s) = i\int_0^L \{A_h\alpha_j(L-z,\omega_s)\hat{m}_{j\sigma}(z,\Omega_{sh}) - A_l^*\beta_j(L-z,\omega_s)\hat{m}_{qx}(z,\Omega_{sh})\}e^{-i\Delta z}dz, \tag{A6}$$

where Δ is given by

$$\Delta = \frac{1}{2}\{k_x(\omega_l) - k_\sigma(\omega_h) + \gamma(P_l - P_h)[1 - \xi_\sigma(0)]\}. \tag{A7}$$

In Eqs. (A1)–(A7), $j,q=x,y$. $q=j$ and $\sigma=x$ for copolarized pumping but $q\neq j$ and $\sigma=y$ for orthogonal pumping.

APPENDIX B: PHOTON FLUX AND PAIR CORRELATION IN DUAL-PUMP CONFIGURATIONS

Equations (38) and (A1)–(A6) can be used to find the general expression for the photon flux and pair correlation. In the case of copolarized pumping, we consider only the case when the photon pairs are created with polarization parallel to the two pumps. In this case, the photon flux, including both spontaneous and stimulated contributions, are found to have the following general form:

$$I_u = \frac{1}{2\pi}\int_{-\infty}^{\infty} |H_u|^2[|\beta_u|^2 + \mathcal{N}(\Omega_{ul})|g_R(\Omega_{ul})|F_l(\omega_u) + \mathcal{N}(\Omega_{uh})|g_R(\Omega_{uh})|F_h(\omega_u)]d\omega_u, \tag{B1}$$

where $u=s$ or i for signal and idler photons. The quantity $F_\mu(\omega) \equiv \int_0^L |f_\mu(z,\omega)|^2 dz$ $(\mu=l,h)$ describes the magnitude of amplified SpRS and f_μ is given by

$$f_{\mu j}(z,\omega_s) = A_\mu\alpha_j(L-z,\omega_s) - A_v^*\beta_j(L-z,\omega_s), \tag{B2}$$

with the polarization subscript j dropped, and where $\mu,v=l,h$ but $\mu\neq v$.

The degree of quantum correlation between the signal and idler photons is obtained from Eqs. (38) and (A1)–(A6) using the definition given in Eq. (26). When the signal and idler are distinguishable with each other $[\bar{\omega}_s \neq \bar{\omega}_i$, Fig. 6(a)], the correlation is given by

$$\rho_c(\tau) = \frac{1}{(2\pi)^2 I_s I_i}\left|\int_{-\infty}^{\infty} \mathcal{H}(\omega_s) \times [\alpha_i\beta_s - \mathcal{N}(\Omega_{sl})|g_R(\Omega_{sl})|\mathcal{F}_l(\omega_s) - \mathcal{N}(\Omega_{sh}) \times |g_R(\Omega_{sh})|\mathcal{F}_h(\omega_s)]e^{-i\omega_s\tau}d\omega_s\right|^2, \tag{B3}$$

where $\mathcal{F}_u(\omega_s) = \int_0^L f_u(z,\omega_s)f_v(z,\omega_i)dz$ with $u,v=l$ or h $(u\neq v)$ and $\omega_i=\omega_l+\omega_h-\omega_s$; its analytical form can be obtained using Eq. (B2).

When the signal and idler photons are indistinguishable on the basis of their frequencies $[\bar{\omega}_s=\bar{\omega}_i$, Fig. 6(b)], the pair correlation for the experimental configuration shown in Fig. 8 can be obtained by using the definition in Eq. (23). Its general form is given by

$$\rho_c(\tau) = \frac{I_s^{-2}}{(2\pi)^2}\left|\int_{-\infty}^{\infty} \mathcal{H}(\omega_s)[\alpha_i\beta_s - \mathcal{N}(\Omega_{sl})|g_R(\Omega_{sl})|\mathcal{F}_l(\omega_s) - \mathcal{N}(\Omega_{sh})|g_R(\Omega_{sh})|\mathcal{F}_h(\omega_s)]e^{-i\omega_s\tau}d\omega_s\right|^2 + \frac{I_s^{-2}}{(2\pi)^2}\left|\int_{-\infty}^{\infty} |H_s|^2[|\beta_s|^2 + \mathcal{N}(\Omega_{sl})|g_R(\Omega_{sl})|F_l(\omega_s) + \mathcal{N}(\Omega_{sh})|g_R(\Omega_{sh})|F_h(\omega_s)]e^{-i\omega_s\tau}d\omega_s\right|^2, \tag{B4}$$

where the first term in Eq. (B4) provides the cross correlation between the signal-idler pair. The second term is very similar to Eq. (24), and it reflects the self-correlation of signal photons.

In the case of orthogonal pumping, the photon fluxes for the x and y polarization components are given by

$$I_{ux} = \frac{1}{2\pi}\int_{-\infty}^{\infty} d\omega_u|H_u|^2\{|\beta_{ux}|^2 + \mathcal{N}(\Omega_{uh})|g_\perp(\Omega_{uh})|F_{hx}(\omega_u) + \mathcal{N}(\Omega_{ul})[|g_a(\Omega_{ul})|F_{lx}(\omega_u) + |g_b(\Omega_{ul})|F'_{lx}(\omega_u)]\}, \tag{B5}$$

$$I_{uy} = \frac{1}{2\pi}\int_{-\infty}^{\infty} d\omega_u|H_u|^2\{|\beta_{uy}|^2 + \mathcal{N}(\Omega_{ul})|g_\perp(\Omega_{ul})|F_{ly}(\omega_u) + \mathcal{N}(\Omega_{uh})[|g_a(\Omega_{uh})|F_{hy}(\omega_u) + |g_b(\Omega_{uh})|F'_{hy}(\omega_u)]\}, \tag{B6}$$

where $F_{uj}(\omega) = \int_0^L |f_{uj}(z,\omega)|^2 dz$, f_{uj} is given by Eq. (B2), and F'_{uj} is defined as

$$F'_{uj}(\omega) = \int_0^L [P_u|\alpha_j(z,\omega)|^2 + P_v|\beta_j(z,\omega)|^2]dz, \tag{B7}$$

with $j=x,y$ and $u,v=l,h$ but $v\neq u$.

Similarly, $\mathcal{P}_{xy}$ and $\mathcal{P}_{yx}(\tau)$ in Eq. (48) are given by

$$\mathcal{P}_{xy}(\tau) = \frac{1}{2\pi}\int_{-\infty}^{\infty} \mathcal{H}(\omega_s)\{\alpha_{iy}\beta_{sx} - \mathcal{N}(\Omega_{sh})|g_\perp(\Omega_{sh})|\mathcal{F}_{hx}(\omega_s) - \mathcal{N}(\Omega_{sl})[|g_a(\Omega_{sl})|\mathcal{F}_{lx}(\omega_s) + |g_b(\Omega_{sl})|\mathcal{F}'_{lx}(\omega_s)]\}e^{-i\omega_s\tau}d\omega_s, \tag{B8}$$

$$\mathcal{P}_{yx}(\tau) = \frac{1}{2\pi}\int_{-\infty}^{\infty} \mathcal{H}(\omega_s)\{\alpha_{ix}\beta_{sy} - \mathcal{N}(\Omega_{sl})|g_\perp(\Omega_{sl})|\mathcal{F}_{ly}(\omega_s) - \mathcal{N}(\Omega_{sh})[|g_a(\Omega_{sh})|\mathcal{F}_{hy}(\omega_s) + |g_b(\Omega_{sh})|\mathcal{F}'_{hy}(\omega_s)]\}e^{-i\omega_s\tau}d\omega_s, \tag{B9}$$

where $\mathcal{F}_{uj}(\omega_s)=\int_0^L f_{uj}(z,\omega_s)f_{vq}(z,\omega_i)dz$ with $\omega_i=\omega_l+\omega_h-\omega_s$, and $\mathcal{F}'_{uj}(\omega_s)$ is defined as

$$\mathcal{F}'_{uj}(\omega_s)=-\int_0^L dz[P_u\alpha_j(z,\omega_s)\beta_q(z,\omega_i)+P_v\beta_j(z,\omega_s)\alpha_q(z,\omega_i)], \tag{B10}$$

where $u,v=l,h$ with $v\neq u$ and $j,q=x,y$ with $q\neq j$.

APPENDIX C: DUAL PUMPING WITH CIRCULAR POLARIZATIONS

In the case of orthogonal pumping with circular SOPs, the noise operators in Eq. (58) are related to those in the basis of linear polarizations as

$$\hat{m}_{\uparrow\uparrow}=\frac{1}{2}[\hat{m}_{xx}+\hat{m}_{yy}+i(\hat{m}_{xy}-\hat{m}_{yx})], \tag{C1}$$

$$\hat{m}_{\downarrow\downarrow}=\frac{1}{2}[\hat{m}_{xx}+\hat{m}_{yy}-i(\hat{m}_{xy}-\hat{m}_{yx})], \tag{C2}$$

$$\hat{m}_{\uparrow\downarrow}=\frac{1}{2}[\hat{m}_{xx}-\hat{m}_{yy}-i(\hat{m}_{xy}+\hat{m}_{yx})], \tag{C3}$$

$$\hat{m}_{\downarrow\uparrow}=\frac{1}{2}[\hat{m}_{xx}-\hat{m}_{yy}+i(\hat{m}_{xy}+\hat{m}_{yx})]. \tag{C4}$$

These four equations together with Eq. (8) can be used to find the commutation relationship for the noise operators in the circular polarization basis.

As SRS-induced power transfer is negligible between orthogonally polarized pumps, Eq. (55) provides solutions for the two pumps similar to Eq. (34) as

$$A_{uj}(z)\approx A_u\exp\{iz[k_j(\omega_u)+\gamma\xi_0P_u+\gamma\xi_q(0)P_v]\}, \tag{C5}$$

where $u,v=l,h$ $(u\neq v)$ and $j,q=\uparrow,\downarrow$ $(j\neq q)$. A_u is the input pump amplitude at ω_u. Using this solution in Eq. (58), we can find the field solutions for the signal and idler waves. They have a form similar to Eq. (38) except that the subscript x and y are replaced by $\uparrow$ and $\downarrow$, respectively. In this case, α_j and β_j $(j=\uparrow,\downarrow)$ are still given by Eqs. (15) and (16) except that A_p^2 is replaced by A_lA_h and η_j is given by either Eq. (59) or Eq. (60). The parametric gain coefficient is found to have the same form as Eq. (A1) but the other parameters are given by

$$\kappa_j=k(\omega_s)+k(\omega_i)-k(\omega_l)-k(\omega_h)+\gamma P_0[\xi_j(\Omega_{sl})+\xi_q(\Omega_{sh})-\xi_\downarrow(0)-\xi_0(0)], \tag{C6}$$

$$K_j=\frac{1}{2}\{k(\omega_s)-k(\omega_i)+\gamma(P_l-P_h)[\xi_j(\Omega_{sl})-\xi_q(\Omega_{sh})]\}, \tag{C7}$$

$$\Phi(L)=\exp\{(i/2)L\{k(\omega_l)+k(\omega_h)+\gamma P_0[\xi_0(0)+\xi_\downarrow(0)]\}\}, \tag{C8}$$

where $j,q=\uparrow,\downarrow$ with $j\neq q$. The accumulated noise operators in Eq. (38) are found to have the same forms as Eqs. (A5) and (A6) except that the subscripts $j,q=\uparrow,\downarrow$ $(j\neq q)$, x and σ are replaced by $\uparrow$ and $\downarrow$, respectively, and Δ is given by

$$\Delta=\frac{1}{2}\{k(\omega_l)-k(\omega_h)+\gamma(P_l-P_h)[\xi_0(0)-\xi_\downarrow(0)]\}. \tag{C9}$$

APPENDIX D: CHSH PARAMETER

In the single pump configuration of Sec. III, a time-multiplexing technique [19] or a polarization-diversity loop [18] is used to construct a polarization-entangled state. In this approach, the signal photon is coupled to the copolarized idler but the two processes at different polarizations are independent of each other.

By using Eqs. (14)–(17), we find that Γ_1, Γ_2, and $\mathcal{E}_+(\tau)$ are given by

$$\Gamma_1(\tau)=\frac{1}{4}[\Delta I_s\Delta I_i+|\mathcal{P}_{xx}(\tau)-\mathcal{P}_{yy}(\tau)|^2], \tag{D1}$$

$$\Gamma_2(\tau)=\frac{1}{4}[\Delta I_s\Delta I_i+|\mathcal{P}_{xx}(\tau)+\mathcal{P}_{yy}(\tau)|^2], \tag{D2}$$

$$\mathcal{E}_+(\tau)=I_{s+}I_{i+}+|\mathcal{P}_{xx}(\tau)|^2+|\mathcal{P}_{yy}(\tau)|^2, \tag{D3}$$

where $I_{u+}=I_{ux}+I_{uy}$ and $\Delta I_u=I_{ux}-I_{uy}$ are total and difference photon fluxes of the two polarization components $(u=s,i)$, respectively, and $\mathcal{P}_{qq}(\tau)\equiv\langle\hat{A}_{sq}(t+\tau)\hat{A}_{iq}(t)\rangle$ $(q=x,y)$ is related to the signal-idler pair correlation, as discussed in Sec. III.

In general, birefringent components are used to construct four EPR Bell states [3,19]. Here we consider one of them, assuming that the two FWM paths have the same phase. As the two FWM paths are nearly identical, $\Gamma_1(\tau)\approx 0$, it is easy to show that the magnitude of $S(\tau)$ is maximized by setting, for example, $\theta_s=\pi/8$, $\theta'_s=-\pi/8$, $\theta_i=0$, and $\theta'_i=-\pi/4$. These values result in the following maximal value:

$$S_m(\tau)=\frac{4\sqrt{2}\Gamma_2(\tau)}{\mathcal{E}_+(\tau)}=\frac{\sqrt{2}[\Delta I_s\Delta I_i+|\mathcal{P}_{xx}(\tau)+\mathcal{P}_{yy}(\tau)|^2]}{I_{s+}I_{i+}+|\mathcal{P}_{xx}(\tau)|^2+|\mathcal{P}_{yy}(\tau)|^2}. \tag{D4}$$

If the pump power is split equally, $I_{ux}=I_{uy}$, $\mathcal{P}_{xx}(\tau)=\mathcal{P}_{yy}(\tau)$, and Eq. (D4) reduces to the simple form given in Eq. (77).

Equations (D4) and (77) remain valid even when orthogonally polarized noise background is present as long as the photon fluxes ΔI_u and I_{u+} in Eq. (D4) include this contribution. Hence $\rho_c(\tau)$ in Eq. (77) should be given as the realistic ratio between the true coincidence counting and accidental one.

The situation is quite similar in the case of two copolarized pumps (see Fig. 6). If the signal and idler are photons are indistinguisable [$\bar{\omega}_s=\bar{\omega}_i$, Fig. 6(b)], the photon self-correlation also contributes to coincidence counting. However, the maximum CHSH parameter is still given by $S_m(\tau)=4\sqrt{2}\Gamma_2(\tau)/\mathcal{E}_+(\tau)$, provided we employ the following expressions:

$$\Gamma_2(\tau) = \frac{1}{4}[(\Delta I_s)^2 + |\mathcal{P}_{xx}(\tau) + \mathcal{P}_{yy}(\tau)|^2 + |\mathcal{P}'_{xx}(\tau) + \mathcal{P}'_{yy}(\tau)|^2], \tag{D5}$$

$$\mathcal{E}_+(\tau) = I_{s+}^2 + |\mathcal{P}_{xx}(\tau)|^2 + |\mathcal{P}_{yy}(\tau)|^2 + |\mathcal{P}'_{xx}(\tau)|^2 + |\mathcal{P}'_{yy}(\tau)|^2, \tag{D6}$$

where $\mathcal{P}'_{qq}(\tau) \equiv \langle \hat{A}^\dagger_{sq}(L,t+\tau)\hat{A}_{sq}(L,t)\rangle$ $(q=x,y)$ is related to the self-correlation of the x-polarized and y-polarized signal photons, respectively. In the optimal case when the pump power is equally split in two polarizations, $S_m(\tau)$ is still given by the simple form of Eq. (77) but where $\rho_c(\tau)$ is now given by Eq. (43).

In the case of orthogonally polarized pumps with linear SOPs (see Figs. 7 and 11), the x-polarized signal is coupled to the y-polarized idler, and vice versa. The two eigenprocesses are also independent of each other.

When the signal and idler are distinguishable from each other $(\bar{\omega}_s \neq \bar{\omega}_i)$, by using Eqs. (38), (A5), and (A6), we find that $\Gamma_1(\tau)$, $\Gamma_2(\tau)$, and $\mathcal{E}_+(\tau)$ are given by

$$\Gamma_1(\tau) = \frac{1}{4}[\Delta I_s \Delta I_i - |\mathcal{P}_{xy}(\tau) + \mathcal{P}_{yx}(\tau)|^2], \tag{D7}$$

$$\Gamma_2(\tau) = \frac{1}{4}[\Delta I_s \Delta I_i - |\mathcal{P}_{xy}(\tau) - \mathcal{P}_{yx}(\tau)|^2], \tag{D8}$$

$$\mathcal{E}_+(\tau) = I_{s+} I_{i+} + |\mathcal{P}_{xy}(\tau)|^2 + |\mathcal{P}_{yx}(\tau)|^2. \tag{D9}$$

Note that $\mathcal{P}_{xy}(\tau)$ and $\mathcal{P}_{yx}(\tau)$ are now given by Eqs. (B8) and (B9) [or by Eqs. (49) and (50) at low pump power levels], respectively. As the two eigenprocesses are nearly identical to each other, $\Gamma_2(\tau) \approx 0$. The magnitude of the CHSH parameter is maximized by setting, for example, $\theta_s = \pi/8$, $\theta'_s = -\pi/8$, $\theta_i = \pi/2$, and $\theta'_i = 3\pi/4$, resulting in

$$S_m(\tau) = \frac{-4\sqrt{2}\Gamma_1(\tau)}{\mathcal{E}_+(\tau)}. \tag{D10}$$

Using Eqs. (D9) and (D7), we find that Eq. (D10) reduces to Eq. (78).

If the signal and idler are identical $(\bar{\omega}_s = \bar{\omega}_i)$ [Fig. 11(c)], self-correlation contributes to coincidence counting. $S_m(\tau)$ is still given by Eq. (D10) under the same angle setting, but $\Gamma_1(\tau)$ and $\mathcal{E}_+(\tau)$ are now modified to become

$$\Gamma_1(\tau) = \frac{1}{4}[(\Delta I_s)^2 - |\mathcal{P}_{xy}(\tau) + \mathcal{P}_{yx}(\tau)|^2 + |\mathcal{P}'_{xx}(\tau) - \mathcal{P}'_{yy}(\tau)|^2], \tag{D11}$$

$$\mathcal{E}_+(\tau) = I_{s+}^2 + |\mathcal{P}_{xy}(\tau)|^2 + |\mathcal{P}_{yx}(\tau)|^2 + |\mathcal{P}'_{xx}(\tau)|^2 + |\mathcal{P}'_{yy}(\tau)|^2. \tag{D12}$$

If narrowband filters are used for the signal, Eqs. (D11) and (D12) reduce to

$$\Gamma_1(\tau) = \frac{1}{4}[(\Delta I_s)^2(1 + |\varphi_s(\tau)|^2) - |\mathcal{P}_{xy}(\tau) + \mathcal{P}_{yx}(\tau)|^2], \tag{D13}$$

$$\mathcal{E}_+(\tau) = I_{s+}^2 + |\varphi_s(\tau)|^2(I_{sx}^2 + I_{sy}^2) + |\mathcal{P}_{xy}(\tau)|^2 + |\mathcal{P}_{yx}(\tau)|^2, \tag{D14}$$

where $\varphi_s(\tau)$ is given by Eq. (25). Because of the symmetry of the two eigenprocesses, their pair correlations are the same, and Eq. (D10) reduces to Eq. (79).

In the case of orthogonally polarized pumps with circular SOPs (see Fig. 12), the two eigenprocesses are $\uparrow_l + \downarrow_h \rightarrow \uparrow_s + \downarrow_i$ and $\uparrow_l + \downarrow_h \rightarrow \downarrow_s + \uparrow_i$, which are independent of each other. As a result, $\Gamma_1(\tau) = 0$. Here we only consider the case when the signal and idler are distinguishable from each other $(\bar{\omega}_s \neq \bar{\omega}_i)$. In this case, $\Gamma_2(\tau)$ and $\mathcal{E}_+(\tau)$ are given by

$$\Gamma_2(\tau) = \mathcal{P}^*_{\uparrow\downarrow}(\tau)\mathcal{P}_{\downarrow\uparrow}(\tau), \tag{D15}$$

$$\mathcal{E}_+(\tau) = I_{s+} I_{i+} + |\mathcal{P}_{\uparrow\downarrow}(\tau)|^2 + |\mathcal{P}_{\downarrow\uparrow}(\tau)|^2, \tag{D16}$$

where $I_{u+} = I_{u\uparrow} + I_{u\downarrow}$ $(u=s,i)$. The magnitude of the CHSH parameter is maximized by setting, for example, $\theta_s = \pi/8$, $\theta'_s = -\pi/8$, $\theta_i = 0$, and $\theta'_i = -\pi/4$, resulting in

$$S_m(\tau) = \frac{2\sqrt{2}[\Gamma_2(\tau) + \Gamma_2^*(\tau)]}{\mathcal{E}_+(\tau)}. \tag{D17}$$

Using Eqs. (D15) and (D16), we find that Eq. (D17) reduces to Eq. (81). Following a similar approach, we can find $S_m(\tau)$ for the case of identical signal and idler $(\bar{\omega}_s = \bar{\omega}_i)$.

[1] N. Gisin, G. Ribordy, W. Tittel, and H. Zbinden, Rev. Mod. Phys. **74**, 145 (2002).

[2] D. C. Burnham and D. L. Weinberg, Phys. Rev. Lett. **25**, 84 (1970).

[3] P. G. Kwiat, K. Mattle, H. Weinfurter, A. Zeilinger, A. V. Sergienko, and Y. Shih, Phys. Rev. Lett. **75**, 4337 (1995).

[4] S. Tanzilli, W. Tittel, M Halder, O. Alibart, P. Baldi, N. Gisin, and H. Zbinden, Nature (London) **437**, 116 (2005).

[5] S. Tanzilli, H. De Riedmatten, W. Tittel, H. Zbinden, P. Baldi, M. De Micheli, D. B. Ostrowsky, and N. Gisin, Electron. Lett. **37**, 26 (2001).

[6] H. Takesue, K. Inoue, O. Tadanaga, Y. Nishida, and M. Asobe, Opt. Lett. **30**, 293 (2005).

[7] M. Fiorentino, P. L. Voss, J. E. Sharping, and P. Kumar, IEEE Photonics Technol. Lett. **14**, 983 (2002).

[8] J. E. Sharping, J. Chen, X. Li, P. Kumar, and R. S. Windeler, Opt. Express **12**, 3086 (2004).

[9] X. Li, J. Chen, P. Voss, J. Sharping, and P. Kumar, Opt. Express **12**, 3737 (2004).

[10] K. Inoue and K. Shimizu, Jpn. J. Appl. Phys., Part 1 **43**, 8048

(2004).
[11] J. G. Rarity, J. Fulconis, J. Duligall, W. J. Wadsworth, and P. St. J. Russell, Opt. Express **13**, 534 (2005).
[12] J. Fulconis, O. Alibart, W. J. Wadsworth, P. St. J. Russell, and J. G. Rarity, Opt. Express **13**, 7572 (2005).
[13] H. Takesue and K. Inoue, Opt. Express **13**, 7832 (2005).
[14] K. F. Lee, J. Chen, C. Liang, X. Li, P. L. Voss, and P. Kumar, Opt. Lett. **31**, 1905 (2006).
[15] J. Fan, A. Dogariu, and L. J. Wang, Opt. Lett. **30**, 1530 (2005).
[16] J. Fan, A. Migdall, and L. J. Wang, Opt. Lett. **30**, 3368 (2005).
[17] J. Fan and A. Migdall, Opt. Express **13**, 5777 (2005).
[18] H. Takesue and K. Inoue, Phys. Rev. A **70**, 031802(R) (2004).
[19] X. Li, P. L. Voss, J. E. Sharping, and P. Kumar, Phys. Rev. Lett. **94**, 053601 (2005).
[20] H. Takesue and K. Inoue, Phys. Rev. A **72**, 041804(R) (2005).
[21] L. J. Wang, C. K. Hong, and S. R. Friberg, J. Opt. B: Quantum Semiclassical Opt. **3**, 346 (2001).
[22] J. Chen, X. Li, and P. Kumar, Phys. Rev. A **72**, 033801 (2005).
[23] O. Alibart, J. Fulconis, G. K. L. Wong, S. G. Murdoch, W. J. Wadsworth, and J. G. Rarity, New J. Phys. **8**, 67 (2006).
[24] P. L. Voss and P. Kumar, Opt. Lett. **29**, 445 (2004); J. Opt. B: Quantum Semiclassical Opt. **6**, S762 (2004).
[25] R. H. Stolen, in *Raman Amplifiers for Telecommunications 1*, edited by M. N. Islam (Springer, New York, 2003), Chap. 2. The Raman spectrum data used in this paper were provided by R. H. Stolen.
[26] R. H. Stolen, J. P. Gordon, W. J. Tomlinson, and H. A. Haus, J. Opt. Soc. Am. B **6**, 1159 (1989).
[27] Q. Lin, F. Yaman, and G. P. Agrawal, Opt. Lett. **31**, 1286 (2006).
[28] L. Boivin, F. X. Kärtner, and H. A. Haus, Phys. Rev. Lett. **73**, 240 (1994).
[29] F. X. Kärtner, D. J. Dougherty, H. A. Haus, and E. P. Ippen, J. Opt. Soc. Am. B **11**, 1267 (1994).
[30] P. D. Drummond, in *Coherence and Quantum Optics VII*, edited by J. H. Eberly, L. Mandel, and E. Wolf (Plenum Press, New York, 1996), p. 323.
[31] R. W. Hellwarth, Prog. Quantum Electron. **5**, 1 (1977).
[32] G. P. Agrawal, *Nonlinear Fiber Optics*, 3rd ed. (Academic, Boston, 2001).
[33] S. J. Carter and P. D. Drummond, Phys. Rev. Lett. **67**, 3757 (1991).
[34] J. H. Shapiro and L. Boivin, Opt. Lett. **20**, 925 (1995).
[35] P. D. Drummond and J. F. Corney, J. Opt. Soc. Am. B **18**, 139 (2001); , **18**, 153 (2001).
[36] P. L. Voss, K. G. Köprülü, and P. Kumar, J. Opt. Soc. Am. B **23**, 598 (2006).
[37] D. J. Dougherty, F. X. Karnter, H. A. Haus, and E. P. Ippen, Opt. Lett. **20**, 31 (1995).
[38] D. Mahgerefteh, D. L. Butler, J. Goldhar, B. Rosenberg, and G. L. Burdge, Opt. Lett. **21**, 2026 (1996).
[39] L. Mandel and E. Wolf, *Optical Coherence and Quantum Optics* (Cambridge University Press, Cambridge, UK, 1995).
[40] S. G. Murdoch, R. Leonhardt, and J. D. Harvey, Opt. Lett. **20**, 866 (1995).
[41] R. J. Kruhlak, G. K. L. Wong, J. S. Y. Chen, S. G. Murdoch, R. Leonhardt, J. D. Harvey, N. Y. Joly, and J. C. Knight, Opt. Lett. **31**, 1379 (2006).
[42] Y. Deng, Q. Lin, F. Lu, G. P. Agrawal, and W. H. Knox, Opt. Lett. **30**, 1234 (2005).
[43] Q. Lin and G. P. Agrawal, Opt. Lett. **29**, 1114 (2004).
[44] C. J. McKinstrie, H. Kogelnik, R. M. Jopson, S. Radic, and A. V. Kanaev, Opt. Express **12**, 2033 (2004).
[45] W. P. Grice and I. A. Walmsley, Phys. Rev. A **56**, 1627 (1997).
[46] T. E. Keller and M. H. Rubin, Phys. Rev. A **56**, 1534 (1997).
[47] K. K. Y. Wong, M. E. Marhic, K. Uesaka, and L. G. Kazovsky, IEEE Photonics Technol. Lett. **14**, 911 (2002).
[48] S. Radic, C. J. McKinstrie, R. M. Jopson, J. C. Centanni, Q. Lin, and G. P. Agrawal, Electron. Lett. **39**, 838 (2003).
[49] T. Tanemura and K. Kikuchi, IEEE Photonics Technol. Lett. **15**, 1573 (2003).
[50] Q. Lin, R. Jiang, C. F. Marki, C. J. McKinstrie, R. Jopson, J. Ford, G. P. Agrawal, and S. Radic, IEEE Photonics Technol. Lett. **17**, 2376 (2005).
[51] Q. Lin and G. P. Agrawal, J. Opt. Soc. Am. B **21**, 1216 (2004).
[52] D. Branning, W. P. Grice, R. Erdmann, and I. A. Walmsley, Phys. Rev. Lett. **83**, 955 (1999).
[53] P. G. Kwiat, W. A. Vareka, C. K. Hong, H. Nathel, and R. Y. Chiao, Phys. Rev. A **41**, 2910 (1990).
[54] Y. H. Shih, A. V. Sergienko, M. H. Rubin, T. E. Kiess, and C. O. Alley, Phys. Rev. A **49**, 4243 (1994).
[55] K. Sanaka, K. Kawahara, and T. Kuga, Phys. Rev. Lett. **86**, 5620 (2001).
[56] J. D. Franson, Phys. Rev. Lett. **62**, 2205 (1989).
[57] Z. Y. Ou, X. Y. Zou, L. J. Wang, and L. Mandel, Phys. Rev. Lett. **65**, 321 (1990).
[58] M. H. Rubin and Y. H. Shih, Phys. Rev. A **45**, 8138 (1990).
[59] J. F. Clauser, M. A. Horne, A. Shimony, and R. A. Holt, Phys. Rev. Lett. **23**, 880 (1969).
[60] D. F. Walls and G. J. Milburn, *Quantum Optics* (Springer-Verlag, Berlin, 1994).